Monthly Notices of the ROYAL ASTRONOMICAL SOCIETY

MNRAS **500,** 4398–4413 (2021) doi:10.1093/mnras/staa3348
Advance Access publication 2020 October 29

Simulated predictions for H I at $z = 3.35$ with the Ooty Wide Field Array (OWFA) – II. Foreground avoidance

Suman Chatterjee [1,2,3]★ Somnath Bharadwaj[1,2] and Visweshwar Ram Marthi [3,4,5]

[1]*Department of Physics, Indian Institute of Technology Kharagpur, Kharagpur - 721 302, India*
[2]*Centre for Theoretical Studies, Indian Institute of Technology Kharagpur, Kharagpur - 721 302, India*
[3]*National Centre for Radio Astrophysics, Tata Institute of Fundamental Research, Post Bag 3, Ganeshkhind, Pune - 411 007, India*
[4]*Canadian Institute for Theoretical Astrophysics, 60 St. George Street, Toronto, ON M5S 3H8, Canada*
[5]*Dunlap Institute for Astronomy & Astrophysics, 50 St. George Street, Toronto, ON M5S 3H4, Canada*

Accepted 2020 October 22. Received 2020 September 24; in original form 2019 November 13

ABSTRACT

Considering the upcoming OWFA, we use simulations of the foregrounds and the $z = 3.35$ H I 21-cm intensity mapping signal to identify the $(k_\perp, k_{\shortparallel})$ modes where the expected 21-cm power spectrum $P(k_\perp, k_{\shortparallel})$ is substantially larger than the predicted foreground contribution. Only these uncontaminated k modes are used for measuring $P(k_\perp, k_{\shortparallel})$ in the "Foreground Avoidance" technique. Though the foregrounds are largely localized within a wedge. we find that the small leakage beyond the wedge surpasses the 21-cm signal across a significant part of the $(k_\perp, k_{\shortparallel})$ plane. The extent of foreground leakage is extremely sensitive to the frequency window function used to estimate $P(k_\perp, k_{\shortparallel})$. It is possible to reduce the leakage by making the window function narrower; however, this comes at the expense of losing a larger fraction of the 21-cm signal. It is necessary to balance these competing effects to identify an optimal window function. Considering a broad class of cosine window functions, we identify a six term window function as optimal for 21-cm power spectrum estimation with OWFA. Considering only the k modes where the expected 21-cm power spectrum exceeds the predicted foregrounds by a factor of 100 or larger, a $5\,\sigma$ detection of the binned power spectrum is possible in the k-ranges $0.18 \leq k \leq 0.3\,\mathrm{Mpc}^{-1}$ and $0.18 \leq k \leq 0.8\,\mathrm{Mpc}^{-1}$ with 1000–2000 and 10^4 h of observation, respectively.

Key words: techniques: interferometric – diffuse radiation – large-scale structure of Universe – cosmology: observations.

1 INTRODUCTION

Intensity mapping with the neutral hydrogen (H I) 21-cm radiation is a promising tool to study the large-scale structures in the post-reionization Universe (Bharadwaj, Nath & Sethi 2001). It holds the potential of measuring the baryon acoustic oscillation (BAO) that is imprinted in the H I 21-cm power spectrum, and the comoving scale of BAO can be used as a standard ruler to constrain the evolution of the equation of state of dark energy (Chang et al. 2008; Wyithe, Loeb & Geil 2008; Masui, McDonald & Pen 2010; Seo et al. 2010). Further, a measurement of just the H I 21-cm power spectrum can also be used to constrain cosmological parameters (Bharadwaj, Sethi & Saini 2009; Visbal, Loeb & Wyithe 2009). Higher order statistics such as the bispectrum holds the prospect of quantifying the non-Gaussianities in the H I 21-cm signal (Ali, Bharadwaj & Pandey 2005; Hazra & Sarkar 2012). Using the H I signal in cross-correlation with the WiggleZ galaxy survey data, the Green Bank Telescope (GBT) has made the first detection of the H I signal in emission at $z \approx 0.8$ (Chang et al. 2010; Masui et al. 2013). Switzer et al. (2013) have constrained the autopower spectrum of the redshifted H I 21-cm radiation from redshift $z \sim 0.8$ with GBT.

The Giant Meterwave Radio Telescope (GMRT; Swarup et al. 1991) is sensitive to the cosmological H I signal from a range of redshifts in the post-reionization era (Bharadwaj & Pandey 2003; Bharadwaj & Ali 2005) and (Ghosh et al. 2011a,b) have carried out preliminary observations towards detecting this signal from $z = 1.32$. The Canadian Hydrogen Intensity Mapping Experiment (CHIME; Newburgh et al. 2014; Bandura et al. 2014) aims to measure the BAO in the redshift range 0.8–2.5. The future Tianlai (Chen 2012, 2015), SKA1-MID (Bull et al. 2015), HIRAX (Newburgh et al. 2016) and MeerKLASS (Santos et al. 2017) also aim to measure the redshifted H I 21-cm signal from the post-reionization era. In this paper, we consider the upcoming Ooty Wide Field Array (OWFA; Subrahmanya, Manoharan & Chengalur 2017a), which aims to measure the H I signal from $z = 3.35$.

The Ooty Radio telescope (ORT; Swarup et al. 1971) is a 530 m long (north–south) and 30 m wide (east–west) offset-parabolic cylinder that is located on a hill whose slope roughly matches the latitude of the station (11°). Effectively, the axis of the cylinder is parallel to the earth's rotation axis, making it equatorially mounted. The telescope is mechanically steerable in the east–west direction by rotating the cylinder about its axis, allowing continuous tracking of a source on the sky. Throughout this paper, we consider observations that track a single field on the sky. This allows the signal from different time instances to be coherently added to increase the signal-to-noise ratio (SNR).

★ E-mail: schatterjee@ncra.tifr.res.in

Table 1. Definitions for some of the symbols used here.

Symbol	Definition	Symbol	Definition
$b \times d$	Aperture dimensions 30 m×1.92 m	$N_{\rm A}$	Number of antennas 264
$\nu_{\rm c}$	Central frequency 326.5 MHz	$\boldsymbol{U}_a$	Different baselines where $a = 1, 2, \ldots, N_{\rm A} - 1$
$B_{\rm bw}$	Bandwidth 39 MHz	$N_{\rm c}$	Number of channels 312
$\Delta\nu$	Channel width 0.125 MHz	ν_n	Different frequency channels where $n = 0, 1, ..., N_{\rm c} - 1$
$N_{\rm r}$	Number of realization of simulations	$N_{\rm p}$	Number of terms in frequency window function
$N_{\rm s}$	Number of time stamps	r	Comoving distance to redshift 3.35, 6.84 Gpc
		$r^{'}$	$\lvert {\rm d}r/{\rm d}\nu\rvert_{\nu=\nu_{\rm c}}$ 11.5 Mpc MHz^{-1}
$t_{\rm obs}$	Observation time	Δt	Integration time
$P_{\rm T}(k_\perp, k_{\shortparallel})$	H I 21-cm power spectrum	$P_{\rm N}(k_\perp, k_{\shortparallel})$	Noise power spectrum
$P_{\rm L}(k_\perp, k_{\shortparallel})$	Foreground leakage power spectrum	$R(k_\perp, k_{\shortparallel})$	$P_{\rm T}(k_\perp, k_{\shortparallel})/P_{\rm L}(k_\perp, k_{\shortparallel})$
$R_{\rm t}$	Threshold value of $R(k_\perp, k_{\shortparallel})$	$\mathcal{R}(R_{\rm t}, t_{\rm obs})$	Ratio of SNR and SNR for MS6 window

The ORT is currently being upgraded to function as an interferometric array the OWFA. This upgrade will result in two concurrent modes namely OWFA PI and PII. OWFA PI will be a linear array of $N_{\rm A} = 40$ antennas each with a rectangular aperture $b \times d$, where $b = 30$ and $d = 11.5$ m. The entire analysis of this paper is restricted to OWFA PII that has a larger number of antennas $N_{\rm A} = 264$, with smaller aperture ($b = 30$ and $d = 1.92$ m) arranged with a spacing d along the north–south axis of the cylinder. The telescope operates at a nominal frequency of $\nu_{\rm c} = 326.5$ MHz. We consider $N_{\rm c} = 312$ frequency channels each of width $\Delta\nu = 0.125$ MHz spanning a bandwidth of $B_{\rm bw} = 39$ MHz (see Table 1).

The details of the antenna and hardware configuration can be found in Prasad & Subrahmanya (2011) and Subrahmanya et al. (2017a,b). Theoretical estimates (Bharadwaj, Sarkar & Ali 2015) predict that it should be possible to measure the amplitude of the 21-cm power spectrum with 150 h of observations using OWFA PII. A more recent study (Sarkar, Bharadwaj & Ali 2017) indicates possible measurement of the 21-cm power spectrum in several different k-bins in the range 0.05–0.3 Mpc^{-1} with 1000 h of observations. Sarkar, Bharadwaj & Sarkar (2018b) have shown that the cross-correlation of the redshifted H I 21-cm signal with OWFA PII with the Ly α forest is detectable in a 200 h integration each in 25 independent fields of view (FoV).

The complex visibilities are the primary quantities measured by any radio-interferometric array like OWFA. It is possible to directly estimate the H I 21-cm power spectrum from the measured visibilities (Bharadwaj & Sethi 2001; Bharadwaj & Ali 2005). Sarkar, Bharadwaj & Marthi (2018a) have proposed and implemented a new technique to estimate the OWFA H I signal visibilities. Galactic and extragalactic foregrounds pose a severe challenge to the H I 21-cm signal detection (Ali, Bharadwaj & Chengalur 2008; Ghosh et al. 2011b). The theoretical estimates (Ali & Bharadwaj 2014) predict that the visibilities measured at OWFA will be dominated by astrophysical foregrounds that are expected to be several orders of magnitude larger than the H I signal. The astrophysical foregrounds are all expected to have a smooth frequency dependence in contrast to the H I signal. With the increasing frequency separation, the H I signal is expected to decorrelate much faster than the foregrounds (Bharadwaj & Pandey 2003), a feature on which most foreground removal techniques rely to distinguish between the foregrounds and the H I signal. Modelling foreground spectra is challenging and is further complicated by the chromatic response of the telescope primary beam. Marthi et al. (2017, hereafter Paper I) have introduced a Multi-frequency Angular Power Spectrum (MAPS) estimator and demonstrated its ability, using an emulator (PROWESS; Marthi 2017), to accurately characterize the foregrounds for OWFA PI.

Several studies have shown that the foreground contributions are expected to be largely confined within a wedge shaped region in the $(k_\perp, k_{\shortparallel})$ plane (Datta, Bowman & Carilli 2010; Morales et al. 2012; Parsons et al. 2012; Trott, Wayth & Tingay 2012; Vedantham, Udaya Shankar & Subrahmanyan 2012). In this work, we focus on a conservative strategy referred to as 'foreground avoidance'. In this strategy, only the k modes where the predicted foreground contamination is substantially below the expected 21-cm signal are used for power spectrum estimation. Ideally, one hopes to use the entire set of k modes outside the foreground wedge for estimating the 21-cm power spectrum. However, there are several factors that cause foreground leakage beyond the foreground wedge. The chromaticity of the various foreground components and also the individual antenna elements causes foreground leakage beyond the wedge. The exact extent of this wedge is still debatable (see Pober et al. 2014 for a detailed discussion). The large OWFA FoV makes it crucial to address the wide-field effects for the foreground predictions for OWFA. On a similar note, the Fourier transform along the frequency axis used to calculate the cylindrical power spectrum introduces artefacts due to the discontinuity in the measured visibilities at the edge of the band. It is possible to avoid this problem by introducing a frequency window function that smoothly falls to zero at the edges of the band. This issue has been studied by Vedantham et al. (2012) and Thyagarajan et al. (2013), who have proposed the Blackman–Nuttall (BN; Nuttall 1981) window function. While the additional frequency window does successfully mitigate the artefacts, it also introduces additional chromaticity that also contributes to foreground leakage beyond the wedge boundary.

In this paper, we have used simulations of the foregrounds and the H I 21-cm signal expected for OWFA PII to quantify the extent of the foreground contamination outside the foreground wedge. The aim is to identify the $(k_\perp, k_{\shortparallel})$ modes that can be used for measuring the 21-cm power spectrum, and to asses the prospects of measuring the 21-cm power spectrum using the foreground avoidance technique. Our all-sky foreground simulations (described in Section 2) incorporate the two most dominant components namely the diffuse Galactic synchrotron emission and the extragalactic point sources. This work improves upon the earlier work (Paper I) by introducing an all-sky foreground model. The simulated foreground visibilities (described in Section 3) incorporate the chromatic behaviour of both the sources and also the instrument. The actual OWFA primary beam pattern is unknown. We have carried out the entire study here using two different models for the primary beam pattern, we expect the actual OWFA beam pattern to be in between the two different scenarios considered here. We have used the 'Simplified Analysis' of Sarkar et al. (2018a) to simulate the H I signal contribution to the visibilities

(also described in Section 3). To estimate the 21-cm power spectrum from the the OWFA visibilities, in Section 4, we introduce and also validate a visibility-based estimator that has been constructed so as to eliminate the noise bias and provide an unbiased estimate of the 3D power spectrum.

Our results (Section 5) show that the foreground leakage outside the wedge is extremely sensitive to the form of the frequency window function used for estimating the 21-cm power spectrum. While the leakage can be reduced by making the window function narrower, this is at the expense of increasing the loss in the 21-cm signal. It is necessary to balance these two competing effects in order to choose the optimal window function. In this paper, we consider a broad class of cosine window functions each with a different number of terms. We introduce a figure of merit, which allows us to quantitatively compare the performance of different window functions, and we use this to determine the optimal window function to estimate the 21-cm power spectrum using OWFA. Considering the optimal window function, we finally quantify the prospects of measuring the 21-cm power spectrum using OWFA. The results are discussed and summarized in Section 6.

We use the fitting formula of Eisenstein & Hu (1999) for the Lambda cold dark matter (ΛCDM) transfer function to generate the initial, linear matter power spectrum. The cosmological parameter values used are as given in Planck Collaboration I (2014): $\Omega_{\rm m} = 0.318$, $\Omega_{\rm b}\,h^2 = 0.022$, $\Omega_{\lambda} = 0.682$, $n_{\rm s} = 0.961$, $\sigma_8 = 0.834$, and $h = 0.67$.

2 SIMULATIONS

The radiation from different astrophysical sources other than the redshifted cosmological H I 21-cm radiation are collectively referred to as foregrounds. The most dominant contributions to the foregrounds at 326.5 MHz, come from the diffuse synchrotron from our own galaxy (diffuse galactic synchrotron emission, DGSE) and the extragalactic radio sources (extragalactic point sources; EPS). The free–free emission from our galaxy and from external galaxies are also larger than the H I 21-cm signal. We exclude accounting the free–free emissions as a separate component in our analysis since they have power-law spectra similar to the other components (Kogut et al. 1996). They are easily subsumed by the uncertainty in the discrete continuum source contribution and they make relatively smaller contributions to the foregrounds.

2.1 The diffuse galactic synchrotron emission

The DGSE arises from the energetic charged particles (produced mostly by supernova explosions) accelerating in the galactic magnetic field (Ginzburg & Syrovatskii 1969). Various observations at 150 MHz (Bernardi et al. 2009; Ghosh et al. 2012; Iacobelli et al. 2013; Choudhuri et al. 2017) have quantified $\mathcal{C}_\ell$ the angular power spectrum of brightness temperature fluctuations of the DGSE. Based on these, we have modelled the DGSE using

$$\mathcal{C}_\ell(\nu) = 513\,{\rm mK}^2 \left(\frac{1000}{\ell}\right)^{2.34} \left(\frac{150\,{\rm MHz}}{\nu}\right)^{5.04}, \qquad (1)$$

where the amplitude and the ℓ power-law index are from Ghosh et al. (2012), whereas for the frequency spectral index, we have used the results from Rogers & Bowman (2008). Various studies indicate that the amplitude and slope have different values in different patches of the sky (e.g. La Porta et al. 2008, Choudhuri et al. 2017), and so also the spectral index (De Oliveira-Costa et al. 2008). These variations will introduce additional angular and frequency structures. However, in our simulations, we have used fixed values across the entire sky.

We simulate the DGSE using the package HEALPIX (Hierarchical Equal Area isoLatitude Pixelization of a sphere; Górski et al. 2005), where we represent the entire sky using 12 582 912 pixels of size 3.435 arcmin. We assume that the brightness temperature fluctuations of the DGSE are a Gaussian random field and used the SYNFAST routine of HEALPIX to generate different statistically independent realizations of the brightness temperature fluctuations at $\nu_{\rm c}$. These were scaled to obtain the brightness temperature fluctuations at the other frequency channels in the observing bandwidth of OWFA. The left panel of Fig. 1 shows a particular realization of the simulated DGSE maps, and the right panel shows a comparison of $\mathcal{C}_\ell$ values estimated from the simulations (in points) and the input model (in solid line) at $\nu_{\rm c}$. We use 20 statistically independent realizations of the DGSE simulations to estimate the mean values and 1σ error bars shown here.

2.2 Extragalactic point sources

The EPS are expected to dominate the 326.5-MHz sky at most of the angular scales of our interest. These sources are a mix of normal galaxies, radio galaxies, quasars, star-forming galaxies, and other objects, which are unresolved by the OWFA. We model the differential source count dN/dS of the sources using the fitting formula given by Ali & Bharadwaj (2014):

$$\frac{{\rm d}N}{{\rm d}S} = \begin{cases} 4000(\frac{S}{1\,{\rm Jy}})^{-1.64}({\rm Jy\,Sr})^{-1} & 3\,{\rm mJy} \le S \le 3\,{\rm Jy} \\ 134(\frac{S}{1\,{\rm Jy}})^{-2.24}({\rm Jy\,Sr})^{-1} & 10\,\mu{\rm Jy} \le S \le 3{\rm mJy}\,, \end{cases} \qquad (2)$$

where they fit the 325 MHz differential source counts measured by Sirothia et al. (2009). This is consistent with the WENSS 327 MHz differential source count (fig. 9 of Rubart & Schwarz 2013). For the sources below 3 mJy, they fit the 1.4 GHz source counts from extremely deep VLA observations (Biggs & Ivison 2006) and extrapolate it to 326.5 MHz. Here we assume that the sources with flux $S > 3$ mJy make the major contribution to foregrounds, and only consider sources with $S > 3$ mJy. We assume that the spectral nature of such sources can be modelled (spectral behaviour) as a power law $S_\nu \propto \nu^\alpha$, where for each source, we randomly assign a value of α drawn from a Gaussian distribution with mean -2.7 and rms $=$ 0.2 (Olivari et al. 2018). The angular clustering of radio sources at low flux densities is not well known. To make an estimate, we use the angular correlation function $w(\theta)$ measured from NVSS, which can be approximated as $w(\theta) \approx (1.0 \pm 0.2) \times 10^{-3}\,\theta^{-0.8}$ (Overzier et al. 2003), for which the angular power spectrum w_ℓ has been calculated to be $w_\ell \approx 1.8 \times 10^{-4}\ell^{-1.2}$ (Blake, Ferreira & Borrill 2004; Olivari et al. 2018). The EPS contribution to the brightness temperature fluctuations can be decomposed into two parts, namely (a) the Poisson fluctuations due to the discrete nature of the sources, and (b) a fluctuation due to the angular clustering of the sources. The simulations were carried out using HEALPIX with the same specifications as mentioned in Section 2.1. Based on the differential source counts (equation 2), we expect 3145 728 sources in the sky map, corresponding to a mean 0.25 sources per pixel. We have simulated 100 times the expected number of sources (mean 25 per pixel), and assigned them flux values that are randomly drawn from the differential source count (equation 2) and whose spectral index values are assigned randomly as discussed earlier. To incorporate the angular clustering, we generate realizations of Gaussian random fluctuations $\delta_{\rm p}$ (p labels the pixels) corresponding to the angular power spectrum w_ℓ. We distribute the simulated sources among the

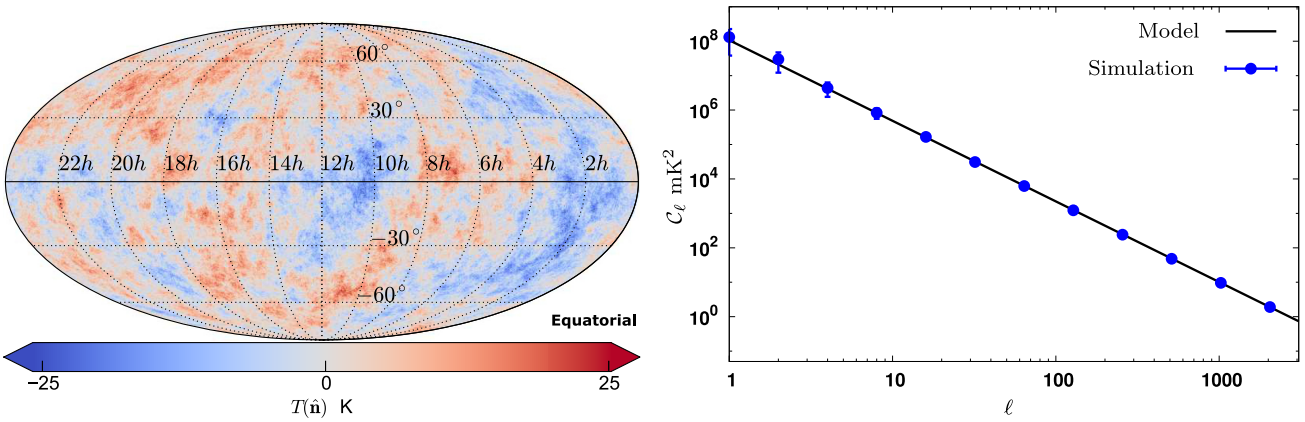

Figure 1. The left panel shows a single realization of the simulated DGSE map for the nominal frequency of $\nu_c = 326.5$ MHz. In the right panel, the line shows the angular power spectrum $\mathcal{C}_\ell$ of the input DGSE model (equation 1) at ν_c, while the points with the error bars are the mean and standard deviation obtained from the simulations.

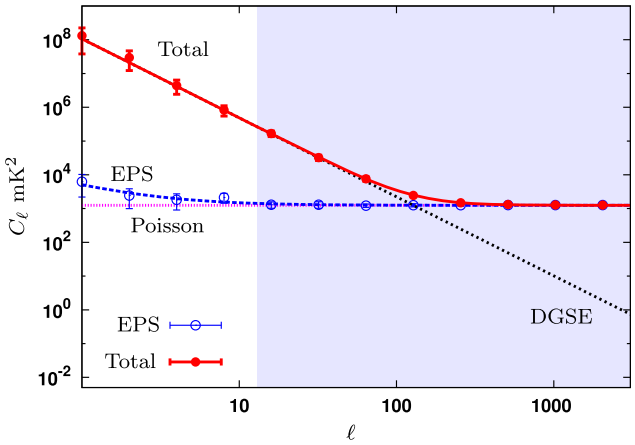

Figure 2. This shows the angular power spectrum $\mathcal{C}_\ell$ of the brightness temperature fluctuations of the foreground components. The hollow and filled circles show the mean EPS and the total foreground (i.e. EPS+DGSE) contributions to $\mathcal{C}_\ell$ with 1σ error bars estimated from 20 statistically independent realizations of the simulations, the analytical predictions are shown in different line-styles as indicated in the figure. The shaded region bounds the ℓ range probed by OWFA PII.

pixels by assigning $25(1 + \delta_p)$ sources from the simulated source list to pixel p, and so on covering all the pixels in the sky map. Finally, we have randomly selected 3145728 sources from the simulated source list. The brightness temperature distribution resulting from these simulated sources now incorporates both the Poisson fluctuation and the angular clustering of the sources.

Fig. 2 shows the mean $\mathcal{C}_\ell(\nu_c)$ along with 1σ error bars estimated from 20 statistically independent realizations of the foregrounds. This is compared with the theoretical predictions for the different components, as well as the predictions for the total expected $\mathcal{C}_\ell$. We see that the DGSE dominates at large angular scales i.e. $\ell < 600$, while the EPS dominates at small angular scales i.e. $\ell \geq 600$.

3 VISIBILITY SIMULATION

OWFA is a linear array of N_A antennas arranged without any intervening gap along the length of a north–south parabolic cylinder. Each antenna has a rectangular aperture of dimension $b \times d = 30\,\mathrm{m} \times 1.92\,\mathrm{m}$ illuminated by four end-to-end linear dipoles (fig. 4 of Paper I). The spacing between the centres of two adjacent antennas also is d, and we have the smallest baselines $\boldsymbol{U}_1 = (d/\lambda)\hat{\boldsymbol{z}}$, where λ is the observing wavelength and we adopt a Cartesian coordinate system that is tied to the telescope with the the unit vectors $\hat{\boldsymbol{z}}$ and $\hat{\boldsymbol{y}}$, respectively, along the length and breadth of the cylinder. The unit vector $\hat{\boldsymbol{x}}$ points perpendicular to the antenna aperture, this direction lies along the celestial equator.

The baselines $\boldsymbol{U}_a = a \times \boldsymbol{U}_1$ measured at OWFA are all multiples of $\boldsymbol{U}_1$ with $a = 1, 2, ..., N_A - 1$. The OWFA baselines have a high degree of redundancy i.e. we have $(N_A - a)$ different antenna pairs that correspond to the same baseline $\boldsymbol{U}_a$. The OWFA visibilities $\mathcal{V}^t(\boldsymbol{U}_a, \nu_n)$ are measured at $n = 0, 1, ..., N_c - 1$ different frequency channels each with a respective central frequency ν_n. Following Paper I, we express the measured visibilities as

$$\mathcal{V}^t(\boldsymbol{U}_a, \nu_n) = \mathcal{M}(\boldsymbol{U}_a, \nu_n) + \mathcal{N}^t(\boldsymbol{U}_a, \nu_n), \tag{3}$$

where $\mathcal{M}(\boldsymbol{U}_a, \nu_n)$ refers to model visibilities originating from the sky signal, and $\mathcal{N}^t(\boldsymbol{U}_a, \nu_n)$ is the additive system noise contribution. Here the label $t = 0, 1, 2, \ldots, N_s - 1$ in $\mathcal{V}^t(\boldsymbol{U}_a, \nu_n)$ denotes distinct measurements of the visibilities each corresponding to a different time stamp and N_s denotes the total number of time stamps. We note that there are several effects like calibration errors, ionospheric fluctuations, and man-made RFI that may also contribute to the measured visibilities in equation (3); however, we do not consider these here. We also consider that a fixed field is being tracked throughout the observation. The model visibility that originates from the sky signal is given by (Perley, Schwab & Bridle 1989)

$$\mathcal{M}(\boldsymbol{U}_a, \nu_n) = Q_{\nu_n} \int \mathrm{d}\Omega_{\hat{\boldsymbol{n}}}\, T(\hat{\boldsymbol{n}}, \nu_n)\, A(\Delta\boldsymbol{n}, \nu_n)\, \mathrm{e}^{-2\pi i \boldsymbol{U}_a \cdot \Delta\boldsymbol{n}}, \tag{4}$$

where, $Q_{\nu_n} = 2k_B/\lambda_n^2$ is the conversion factor from brightness temperature to specific intensity in the Rayleigh–Jeans limit, $T(\hat{\boldsymbol{n}}, \nu_n)$ is the brightness temperature distribution on the sky along the direction of the unit vector $\hat{\boldsymbol{n}}$ that has sky coordinates (RA, Dec.) $= (\alpha, \delta)$, $\mathrm{d}\Omega_{\hat{\boldsymbol{n}}}$ is the elemental solid angle in the direction $\hat{\boldsymbol{n}}$, and $\Delta\boldsymbol{n} = \hat{\boldsymbol{n}} - \hat{\boldsymbol{m}}$, where $\hat{\boldsymbol{m}}$ is the unit vector in the pointing direction of the antennas, which also corresponds to x. Throughout this work, we assume that $\hat{\boldsymbol{m}}$ points towards the position (RA, Dec.) $= (0, 0)$ on the sky.

The model visibilities $\mathcal{M}(\boldsymbol{U}_a, \nu_n)$ can further be considered to be the sum of two parts,

$$\mathcal{M}(\boldsymbol{U}_a, \nu_n) = \mathcal{F}(\boldsymbol{U}_a, \nu_n) + \mathcal{S}(\boldsymbol{U}_a, \nu_n)\,, \tag{5}$$

which refer to the the foreground and the H I signal, respectively.

The foreground contribution $\mathcal{F}(\boldsymbol{U}_a, \nu_n)$ is highly sensitive to the telescope's primary beam pattern (Berger et al. 2016). The actual OWFA primary beam pattern $A(\Delta\boldsymbol{n}, \nu_n)$ is currently unknown, and we have considered two different possibilities for the predictions presented here. The first model for $A(\Delta\boldsymbol{n}, \nu_n)$ (Table 2) is based on the simplest assumption that the OWFA antenna aperture is uniformly illuminated by the dipole feeds, which results in the 'Uniform' sinc-squared primary beam pattern considered in several earlier works (Ali & Bharadwaj 2014; Paper I; Chatterjee & Bharadwaj 2018b). In reality, the actual illumination pattern is expected to fall away from the aperture centre, resulting in a wider FoV as compared to the uniform illumination. In order to assess how this affects the foreground predictions and foreground mitigation, we have considered a 'Triangular' illumination pattern (Fig. 3) for which we have a broader sinc-power-four primary beam pattern (Table 2).

Considering both the uniform and the triangular beam patterns, Fig. 3 shows the variation of $A(\Delta\boldsymbol{n}, \nu)$ with δ (i.e. along the north–south direction) for fixed $\alpha = 0$ and $\nu = \nu_c$. Comparing the two beam patterns, we find that the uniform main lobe subtends $\sim\pm24^\circ$ (FWHM), whereas this is approximately double $\sim\pm35^\circ$ (FWHM) for triangular. The number of side lobes is also found to decrease from uniform to triangular. The uniform and triangular beam patterns represent two extreme cases, and the actual OWFA beam pattern will possibly be somewhere in between these two extreme cases both in terms of the extent of the main lobe and the number of side lobes.

We use the simulated foreground maps (Section 2) to compute $\mathcal{F}(\boldsymbol{U}_a, \nu_n)$ using

$$\mathcal{F}(\boldsymbol{U}_a, \nu_n) = Q_{\nu_n}\, \Delta\Omega_{\rm pix} \sum_{\rm p} T(\alpha_{\rm p}, \delta_{\rm p}, \nu_n) \times A(\alpha_{\rm p}, \delta_{\rm p}, \nu_n) {\rm e}^{-2\pi i U_a (\sin\delta_{\rm p})}\,, \quad (6)$$

where $\Delta\Omega_{\rm pix}$ is the solid angle subtended by each simulation pixel. The pixels in the simulated maps are labeled using p with corresponding $(\mathrm{RA, DEC})_{\rm p} = (\alpha_{\rm p}, \delta_{\rm p})$ and the sum is over all the pixels in the simulation.

Considering $\mathcal{S}(\boldsymbol{U}_a, \nu_n)$, the H I signal contribution to the model visibilities, we have simulated these using the flat-sky approximation (FSA). An earlier work (Chatterjee & Bharadwaj 2018b) has carried out a full spherical harmonic analysis for OWFA to find that the differences from the FSA are at most within 10 per cent at the few smallest baselines and they are much smaller at the other larger baselines. Using $\Delta\boldsymbol{n} = \boldsymbol{\theta}$, which is now a 2D vector on the plane of the sky, equation (4) reads

$$\mathcal{S}(\boldsymbol{U}_a, \nu_n) = Q_{\nu_n} \int {\rm d}^2\boldsymbol{\theta}\, T(\boldsymbol{\theta}, \nu_n)\, A(\boldsymbol{\theta}, \nu_n)\, {\rm e}^{-2\pi i\, \boldsymbol{U}_a\cdot\boldsymbol{\theta}}\,, \quad (7)$$

whereby $\mathcal{S}(\boldsymbol{U}_a, \nu_n)$ is the Fourier transform of $[Q_{\nu_n}\, T(\boldsymbol{\theta}, \nu_n)\, A(\boldsymbol{\theta}, \nu_n)]$. We can express this as a convolution (Ali & Bharadwaj 2014),

$$\mathcal{S}(\boldsymbol{U}_a, \nu_n) = Q_{\nu_n} \int {\rm d}^2\boldsymbol{U}'\, \tilde{a}(\boldsymbol{U}_a - \boldsymbol{U}', \nu_n)\, \tilde{T}(\boldsymbol{U}', \nu_n)\,, \quad (8)$$

where $\tilde{T}(\boldsymbol{U}', \nu)$ is now the Fourier transform of $T(\boldsymbol{\theta}, \nu)$, and the aperture power pattern $\tilde{a}(\boldsymbol{U}, \nu) = \int {\rm d}^2\boldsymbol{\theta}\, {\rm e}^{-2\pi i \boldsymbol{U}\cdot\boldsymbol{\theta}}\, A(\boldsymbol{\theta}, \nu)$ (Table 2).

In a recent work, Sarkar et al. (2018a) have proposed an analytic technique to simulate $\mathcal{S}(\boldsymbol{U}_a, \nu_n)$ the H I signal contribution to the visibilities, which is based on the FSA. Here we have used the 'Simplified Analysis' presented in section 2 of Sarkar et al. (2018a). This uses the eigenvalues and the eigenvectors of the predicted two-visibility correlation matrix $S_2(\boldsymbol{U}_a, \nu_n, \nu_{n'}) = \langle \mathcal{S}(\boldsymbol{U}_a, \nu_n)\, \mathcal{S}^*(\boldsymbol{U}_a, \nu_{n'})\rangle$ to simulate multiple statistically independent realizations of $\mathcal{S}(\boldsymbol{U}_a, \nu_n)$. The simplified analysis used here ignores the correlation between the H I signal at adjacent baselines and also the non-ergodic nature of the H I visibility signal along the frequency axis, both of these have however been included in the 'Generalized Analysis' presented in Sarkar et al. (2018a). We note that it is necessary to diagonalize the entire covariance matrix between the visibilities at all the baselines and frequency channels in order to incorporate the correlations between the H I signal at the adjacent baselines. This is computationally intensive and we have avoided this by adopting the simplified analysis that considers each baseline separately significantly reducing the dimension of the covariance matrix.

The two-visibility correlation $S_2(\boldsymbol{U}_a, \nu_n, \nu_{n'})$ is related to the 21-cm brightness temperature power spectrum $P_{\rm T}(\boldsymbol{k})$ (Bharadwaj & Sethi 2001; Bharadwaj & Ali 2005). For OWFA, we have (Ali & Bharadwaj 2014)

$$S_2(\boldsymbol{U}_a, \nu_n, \nu_{n'}) = Q^2_{\nu_c} \int \frac{{\rm d}^3k}{(2\pi)^3}\, |\tilde{a}(\boldsymbol{U}_a - \frac{\boldsymbol{k}_\perp r}{2\pi}, \nu_c)|^2 \times P_{\rm T}(\boldsymbol{k}_\perp, k_\parallel)\, {\rm e}^{ir'k_\parallel(\nu_{n'}-\nu_n)}\,. \quad (9)$$

Here $\boldsymbol{k}_\perp$, which is the component of a 3D wave vector $\boldsymbol{k}$ perpendicular to the line of sight, can be associated with the baselines $\boldsymbol{U}$ available at OWFA as $\boldsymbol{k}_\perp = 2\pi\boldsymbol{U}/r$, where $r = 6.84\,$Gpc is the comoving distance to $z = 3.35$, and $r' = |{\rm d}r/{\rm d}\nu|_{\nu=\nu_c} = 11.5\,\mathrm{Mpc\,MHz^{-1}}$ sets the conversion scale from the frequency separation to comoving distance in the radial direction. Here $k_{\shortparallel}$ is the line-of-sight component of a 3D wave vector $\boldsymbol{k}$.

The H I 21-cm brightness temperature power spectrum $P_{\rm T}(k_\perp, k_{\shortparallel})$ is modelled as (Ali & Bharadwaj 2014)

$$P_{\rm T}(k_\perp, k_\parallel) = \bar{T}^2 b^2_{\rm HI}\, \bar{x}^2_{\rm HI}\, [1 + \beta\mu^2]^2 P(k)\,, \quad (10)$$

where $\mu = k_{\shortparallel}/k$, $\bar{T} = 4.0\,\mathrm{mk}(1+z)^2\left(\Omega_{\rm b}h^2/0.02\right)(0.7/h)(H_0/H(z))$, $b_{\rm HI} = 2$ is the linear bias, $\bar{x}_{\rm HI} = 2.02\times10^{-2}$ is the mean neutral hydrogen fraction, and $P(k)$ is the power spectrum of the underlying dark matter density distribution. The term $(1 + \beta\mu^2)$ arises due to of the effect of H I peculiar velocities, and $\beta = f(\Omega)/b_{\rm HI}$ is the linear redshift distortion parameter, where $f(\Omega)$ is the dimensionless linear growth rate. We use $\beta = 0.493$ and $f(\Omega) = 0.986$ throughout this paper. It is worth mentioning that, detailed simulations (Castorina & Villaescusa-Navarro 2017; Sarkar & Bharadwaj 2018; Villaescusa-Navarro et al. 2018; Modi et al. 2019) predict that the non-linear effects due the redshift-space distortion becomes significant at high $k_{\shortparallel}$ modes. These non-linearities and the shot noise present at high k modes are not included in the 21-cm power spectrum model considered here (equation 10). However, we expect those high k modes ($k > 1.0\,\mathrm{Mpc^{-1}}$) to be noise dominated and their contribution to the SNR is expected to be small.

The noise contribution $\mathcal{N}^t(\boldsymbol{U}_a, \nu_n)$ in each visibility is assumed to be an independent complex Gaussian random variable with zero mean. The real part (or equivalently the imaginary part) of the noise contribution has an rms fluctuation,

$$\sigma_{\rm N}(\boldsymbol{U}_a) = \frac{\sqrt{2}\, k_{\rm B}\, T_{\rm sys}}{\eta\, A\, \sqrt{\Delta\nu\, \Delta t\, (N_{\rm A} - a)}}\,, \quad (11)$$

where $T_{\rm sys}$ is the total system temperature, $k_{\rm B}$ is the Boltzmann constant, $A = b \times d$ is the physical collecting area of each antenna, η is the aperture efficiency (Table 2) with $\lambda^2/\eta A = \int A(\boldsymbol{\theta}, \nu)\, {\rm d}^2\theta$, and $\Delta t = 16\,$s is the correlator integration time. The OWFA baselines are highly redundant (Ali & Bharadwaj 2014; Subrahmanya et al. 2017b), and the factor $1/\sqrt{(N_{\rm A} - a)}$ in $\sigma_{\rm N}(\boldsymbol{U}_a)$ accounts for the

Table 2. Here Δn_y, U_y, and Δn_z, U_z are, respectively, the y and z components of $\Delta \boldsymbol{n}$ and $\boldsymbol{U}$.

Illumination	Uniform	Triangular
Primary beam pattern $A(\Delta \boldsymbol{n}, \nu) =$	$\mathrm{sinc}^2\left(\pi b\, \Delta n_y/\lambda\right) \mathrm{sinc}^2\left(\pi d\, \Delta n_z/\lambda\right)$	$\mathrm{sinc}^4\left(\pi b\, \Delta n_y/2\lambda\right) \mathrm{sinc}^4\left(\pi d\, \Delta n_z/2\lambda\right)$
Aperture power pattern $\tilde{a}(\boldsymbol{U}, \nu) =$	$\left(\lambda^2/bd\right)\ \Lambda\left(U_y\lambda/b\right) \Lambda\left(U_z\lambda/d\right)$	$\left(64\lambda^2/bd\right)\ G\left(U_y\lambda/b\right) G\left(U_z\lambda/d\right)$
	$\Lambda(x) = \begin{cases} 1-\lvert x\rvert & \text{for } \lvert x\rvert < 1 \\ 0 & \text{for } \lvert x\rvert \geq 1 \end{cases}$	$G(x) = \begin{cases} 1/6 - \lvert x\rvert^2 + \lvert x\rvert^3 & \text{for } \lvert x\rvert < 1/2 \\ 1/3 - \lvert x\rvert + \lvert x\rvert^2 - \lvert x\rvert^3/3 & \text{for } \lvert x\rvert \geq 1/2 \\ 0 & \text{for } \lvert x\rvert \geq 1 \end{cases}$
FWHM, η, $\tilde{\eta}$	$1.55^\circ \times 24^\circ$, 1, 32.49	$2.25^\circ \times 35^\circ$, 9/16, 19.86

Notes. FWHM is the full width at half-maximum of $A(\Delta \boldsymbol{n}, \nu)$. η (equation 11) and $\tilde{\eta}$(equation A3) are the aperture efficiency and a dimensionless factor, respectively.

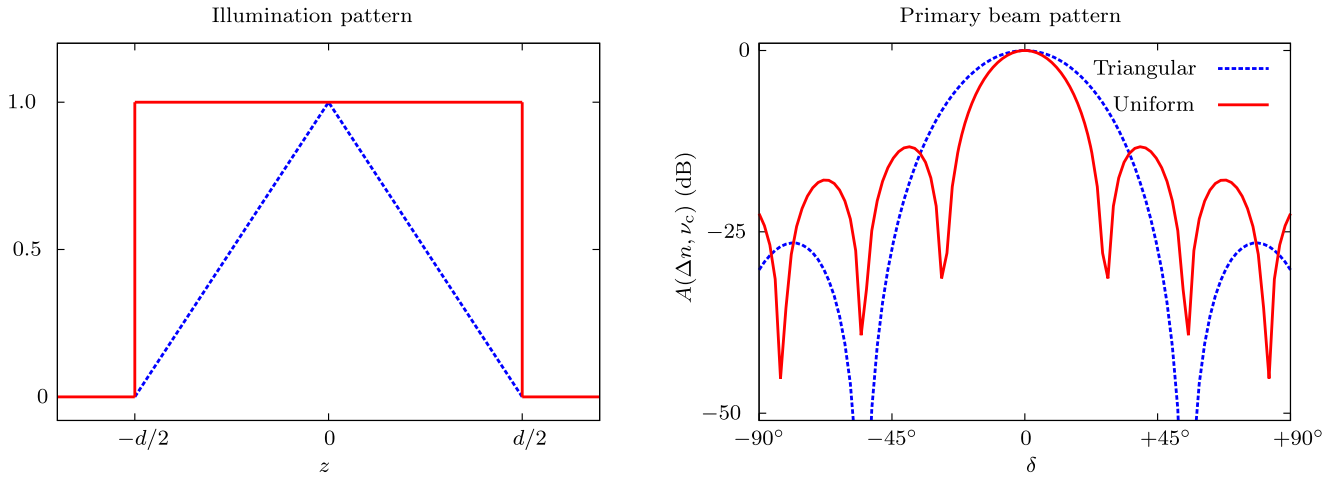

Figure 3. The left panel shows the uniform (red solid line) and triangular (blue dashed line) illumination patterns considered here. The right panel shows the corresponding primary beam patterns (Table 2) along the north–south direction.

redundancy in the baseline distribution. We expect $T_{\rm sys}$ to have a value around 150 K, and we use this value for the estimates presented here.

4 3D POWER SPECRTUM ESTIMATION

We now discuss how the measured visibilities $\mathcal{V}^t\left(\boldsymbol{U}_a, \nu_n\right)$ are used to estimate the 3D power spectrum $P(\boldsymbol{k}_{\perp a}, k_{\parallel m})$. Considering a particular baseline $\boldsymbol{U}_a$ and frequency ν_n, the different time stamps $\mathcal{V}^t\left(\boldsymbol{U}_a, \nu_n\right)$ contain the same sky signal, only the system noise is different. We first average over the different time stamps to reduce the data volume ,

$$\bar{\mathcal{V}}\left(\boldsymbol{U}_a, \nu_n\right) = \frac{1}{N_{\rm s}} \sum_{t=0}^{N_{\rm s}-1} \mathcal{V}^t\left(\boldsymbol{U}_a, \nu_n\right) , \tag{12}$$

here $N_{\rm s}$ denotes the total number of time stamps. The visibilities $\bar{\mathcal{V}}\left(\boldsymbol{U}_a, \nu_n\right)$ are then Fourier transformed along the frequency axis to obtain the visibilities $v^{\rm f}\left(\boldsymbol{U}_a, \tau_m\right)$ in delay space (Morales & Hewitt 2004),

$$v^{\rm f}\left(\boldsymbol{U}_a, \tau_m\right) = (\Delta\nu) \sum_{n=0}^{N_{\rm c}-1} \mathrm{e}^{2\pi i \tau_m \nu_n} F(\nu_n) \bar{\mathcal{V}}\left(\boldsymbol{U}_a, \nu_n\right) , \tag{13}$$

where the delay variable τ_m takes values $\tau_m = m/B_{\rm bw}$ with $-N_{\rm c}/2 < m \leq N_{\rm c}/2$. The Fourier transform here assumes that the visibility signal is periodic in frequency with a period equal to the bandwidth $B_{\rm bw}$. The measured visibilities $\bar{\mathcal{V}}\left(\boldsymbol{U}_a, \nu_n\right)$, however, do not satisfy this requirement. This introduces a discontinuity in the values of the visibilities and also their derivatives at the edge of the frequency band. As noted in several earlier works (Vedantham et al. 2012; Thyagarajan et al. 2013), these discontinuities introduce artefacts that result in foreground leakage outside the foreground wedge. In addition to this, several other features like the frequency dependence of both the foreground sources and the telescope's primary beam pattern also contribute to the foreground leakage. However, in this paper, we entirely focus on the leakage arising from the discontinuities at the boundary of the frequency band. The leakage from these discontinuities can be reduced (Vedantham et al. 2012) by introducing $F(\nu)$ (equation 13), which is a frequency window function that smoothly falls to zero at the edges of the band making the product $[F(\nu_n)\, \bar{\mathcal{V}}\left(\boldsymbol{U}_a, \nu_n\right)]$ effectively continuous at the edge of the band. Earlier works (Vedantham et al. 2012; Thyagarajan et al. 2013) show that the BN (Nuttall 1981) window function is a promising candidate for power spectrum estimation, and this is expected to reduce the foreground leakage by seven to eight orders of magnitude. However, discontinuities in the various derivatives persist and, as we shall see later, the BN window function fails to reduce the foreground leakage to a level below the H I signal expected at OWFA. In order to investigate if this problem can be overcome by considering other window functions, we have considered a broader set of cosine window functions ,

$$F(\nu_n) = \sum_{p=0}^{N_{\rm p}-1} (-1)^p\, A_{\rm p}\, \cos\left(\frac{2np\pi}{N_{\rm c}-1}\right) , \tag{14}$$

each having different coefficients $A_{\rm p}$ and number of terms $N_{\rm p}$. Since the band is divided into an even number ($N_{\rm c}$) of frequency channels, the channel with index $N_{\rm c}/2$ is considered as the centre frequency where the window function peaks. Note that this is equivalent to DFT-even (see e.g. Harris 1978). Here we have considered the Blackman–

Table 3. The coefficients of the different window functions used in this work.

Coefficient	The cosine frequency window functions $F(\nu_n)$				
A_p	BN	BH4	MS5	MS6	MS7
	($N_p = 4$)	($N_p = 4$)	($N_p = 5$)	($N_p = 6$)	($N_p = 7$)
A_0	3.6358×10^{-1}	3.5875×10^{-1}	3.2321×10^{-1}	2.9355×10^{-1}	2.7122×10^{-1}
A_1	4.8918×10^{-1}	4.8829×10^{-1}	4.7149×10^{-1}	4.5193×10^{-1}	4.3344×10^{-1}
A_2	1.3659×10^{-1}	1.4128×10^{-1}	1.7553×10^{-1}	2.0141×10^{-1}	2.1800×10^{-1}
A_3	1.0641×10^{-2}	1.1680×10^{-2}	2.8496×10^{-2}	4.7926×10^{-2}	6.5785×10^{-2}
A_4			1.2613×10^{-3}	5.0261×10^{-3}	$1.076\,18 \times 10^{-2}$
A_5				1.3755×10^{-4}	7.7001×10^{-4}
A_6					1.3680×10^{-5}

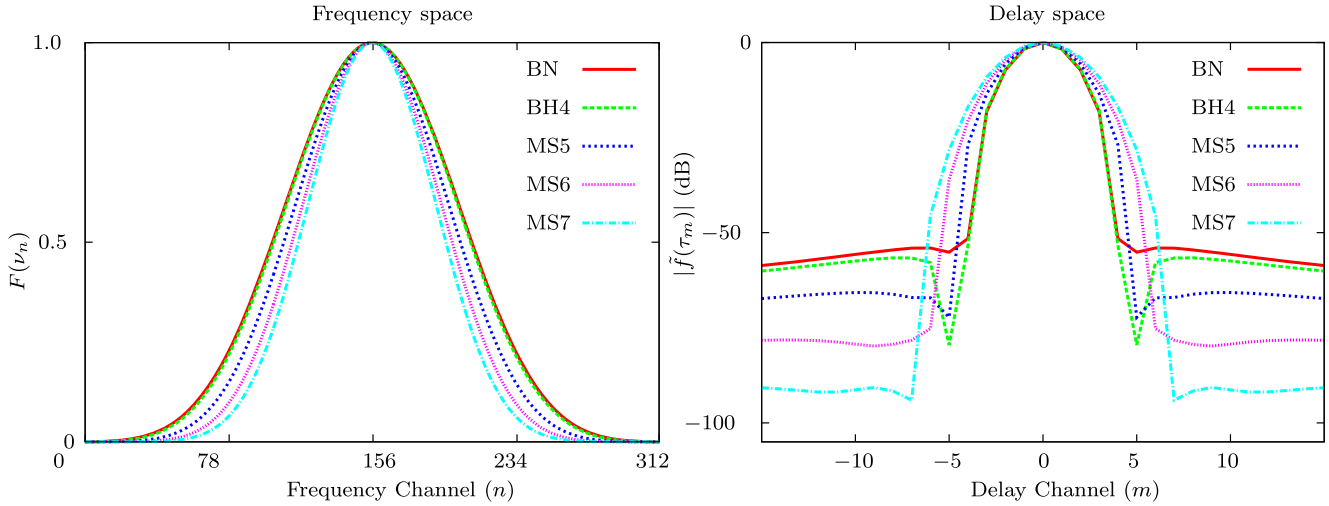

Figure 4. The left panel shows the window functions $F(\nu_n)$ (mentioned in the legend) as a function of channel number n, and the right panel shows the $\tilde{f}(\tau)$ for a small number of delay channels. $\tilde{f}(\tau)$ is normalized to unity at the central delay channel.

Harris four-term window function (BH4), and a family of minimum sidelobe (MS) window functions (MS5, MS6, and MS7). Of these, the BN (Paul et al. 2016) and BH4 (Eastwood et al. 2019) have been used extensively in recent observational studies. Table 3 shows the coefficients (Albrecht 2001) of these window functions considered here.

The left panel of Fig. 4 shows the different window functions $F(\nu)$ considered here. As discussed earlier, we see that the window function smoothly goes down to zero towards the edge of the band. An immediate consequence of introducing the window function $F(\nu)$ is the loss of signal, primarily towards the edge of the frequency band. Considering the window functions $F(\nu)$ in the order shown in Table 3, we see that the $F(\nu)$ gets successively narrower as we move from BN to MS7. We expect the suppression at the edge of the band to be more effective as the window function gets narrower; however, this comes at an expanse of increasing sensitivity loss.

Considering the delay space visibilities $v(\boldsymbol{U}_a, \tau_m)$ without the window function (i.e. $F(\nu) = 1$ in equation 13), we have (Choudhuri et al. 2016)

$$v^{\rm f}(\boldsymbol{U}_a, \tau_m) = \frac{1}{B_{\rm bw}} \sum_{m'=-N_{\rm c}/2}^{N_{\rm c}/2-1} \tilde{f}(\tau_m - \tau_{m'})\, v(\boldsymbol{U}_a, \tau_{m'})\ . \tag{15}$$

We see that $v^{\rm f}(\boldsymbol{U}_a, \tau_m)$ is related to $v(\boldsymbol{U}_a, \tau_m)$ through a convolution with $\tilde{f}(\tau_m)$, which is the Fourier transform of the frequency window $F(\nu)$. This convolution smoothens out the signal over the width of $\tilde{f}(\tau_m)$. Considering the H I signal, the delay space visibilities $v(\boldsymbol{U}_a, \tau_m)$ and $v(\boldsymbol{U}_a, \tau_{m'})$ at two different delay channels τ_m and $\tau_{m'}$ are predicted to be uncorrelated (e.g. Choudhuri et al. 2016). The convolution in equation (15) however introduces correlations in $v^{\rm f}(\boldsymbol{U}_a, \tau_m)$ at two different values of the delay channel, the extent of this correlation is restricted within the width of $\tilde{f}(\tau_m)$. The right-hand panel of Fig. 4 shows the amplitude of $\tilde{f}(\tau_m)$ for the different window functions considered here. We see that $\tilde{f}(\tau_m)$ peaks at $m = 0$, and the values of $\tilde{f}(\tau_m)$ are very small beyond the primary lobe, which is typically a few delay channels wide. This primary lobe of $\tilde{f}(\tau_m)$ gets successively wider as we move from BN to MS7, i.e. the window function $F(\nu)$ gets successively narrower. The BN window function has the narrowest $\tilde{f}(\tau_m)$ and $v^{\rm f}(\boldsymbol{U}_a, \tau_m)$ will be correlated upto $m \approx \pm 4$, whereas this extends to $m \approx \pm 7$ for MS7, which is the widest in delay space. The finite width of $\tilde{f}(\tau_m)$ also leads to a loss of H I signal at the smallest τ_m values that correspond to the largest frequency separations. Fig. 4 illustrates the fact that $\tilde{f}(\tau_m)$ widens and this loss in H I signal increases as we move from the BN to the MS7 window function.

The delay space visibility $v^{\rm f}(\boldsymbol{U}_a, \tau_m)$ is related to the H I 21-cm brightness temperature fluctuation $\Delta T_b(\boldsymbol{k}_{\perp a}, k_{\parallel m})$, where $\boldsymbol{k}_{\perp a} = 2\pi \boldsymbol{U}_a / r$ and $k_{\parallel m} = 2\pi \tau_m / r'$ (Morales & Hewitt 2004), and we can use this to estimate $P(\boldsymbol{k}_{\perp a}, k_{\parallel m})$, the 3D power spectrum of the sky signal. Considering the autocorrelation of $v^{\rm f}(\boldsymbol{U}_a, \tau_m)$, we have

$$\langle |v^{\rm f}(\boldsymbol{U}_a, \tau_m)|^2 \rangle = C_F^{-1} \left[P(\boldsymbol{k}_{\perp a}, k_{\parallel m}) + P_{\rm N}(\boldsymbol{k}_{\perp a}, k_{\parallel m}) \right]\ , \tag{16}$$

with

$$C_F^{-1} = \frac{\Delta\nu \ \sum_n |F(\nu_n)|^2 [Q^2_{\nu_c} \ \int \mathrm{d}^2\boldsymbol{U} \, |\tilde{a}\,(\boldsymbol{U}, \nu_c)\,|^2]}{r^2\, r'} \,, \tag{17}$$

and the noise power spectrum is

$$P_{\rm N}(\boldsymbol{k}_{\perp a}, k_{\parallel m}) = C_F \left(\frac{\Delta\nu}{N_{\rm s}}\right)^2 \sum_{n=0}^{N_{\rm c}-1} \sum_{t=0}^{N_{\rm s}-1} \langle |\mathcal{N}^t(\boldsymbol{U}_a, \nu_n)|^2 \rangle \, |F(\nu_n)|^2 \,. \tag{18}$$

The angular brackets $\langle \ldots \rangle$ here denote an ensemble average over different random realizations of the H I 21-cm signal. We can use $|v^{\rm f}\,(\boldsymbol{U}_a, \tau_m)\,|^2$ to estimate the H I 21-cm power spectrum $P(\boldsymbol{k}_{\perp a}, k_{\parallel m})$ except for the term $P_{\rm N}(\boldsymbol{k}_{\perp a}, k_{\parallel m})$, which arises due to the system noise (equation 3) in the measured visibilities. This introduces a positive noise bias that needs to be accounted for before we can use equation (16) to estimate $P(\boldsymbol{k}_{\perp a}, k_{\parallel m})$.

We use equation (16) to define $\hat{P}\,(\boldsymbol{U}_a, \tau_m)$ the 3D power spectrum estimator as

$$\hat{P}\,(\boldsymbol{U}_a, \tau_m) = C_F \, [|v^{\rm f}\,(\boldsymbol{U}_a, \tau_m)\,|^2 - \left(\frac{\Delta\nu}{N_{\rm s}}\right)^2 \sum_{n=0}^{N_{\rm c}-1} \sum_{t=0}^{N_{\rm s}-1} |\mathcal{V}^t\,(\boldsymbol{U}_a, \nu_n)\,|^2 |F(\nu_n)|^2] \,. \tag{19}$$

The second term in the right-hand side of equation (19) is introduced to exactly subtract out the noise bias in equation (16). The estimator $\hat{P}\,(\boldsymbol{U}_a, \tau_m)$ therefor provides an unbiased estimate of the power spectrum, and we have

$$P(\boldsymbol{k}_{\perp a}, k_{\parallel m}) = \langle \hat{P}\,(\boldsymbol{U}_a, \tau_m) \rangle \,. \tag{20}$$

In addition to the noise bias, some signal also is subtracted out; however, the fraction of the total visibility correlation signal that is lost is of the order of $\sim 1/N_{\rm s}$, which is extremely small for a long observation. For example, we have $N_{\rm s} \sim 10^5$ for $t_{\rm obs} = 1000$ h of observation with an integration time of $\Delta t = 16$ s. It is worth noting that the correlation between the adjacent baselines can also be used to obtain additional estimates of the power spectrum (Ali & Bharadwaj 2014); however, we have not considered this possibility here. Appendix A presents analytical expressions for the variance of the estimator; this is useful for predicting the uncertainty in the estimated power spectrum.

4.1 Validating the estimator

To validate the H I signal simulations and the 3D power spectrum estimator, we have carried out simulations of the H I signal visibilities using the prescription described in Section 3 considering both the uniform and the triangular illuminations. For both cases, we have simulated $N_{\rm r} = 1000$ statistically independent realizations of the H I signal visibilities including the system noise component. To reduce the data volume and the computation, we have considered a total observation time of $t_{\rm obs} = 1000$ h with an integration time of $\Delta t = 1$ h for the uniform illumination, and $t_{\rm obs} = 10\,000$ h with $\Delta t = 10$ h for the triangular illumination respectively. In both cases we have $N_{\rm s} = 1000$, which implies that we have $1/N_{\rm s} = 0.1$ per cent loss in the visibility correlation due to the term that cancels out the noise bias. As mentioned earlier, we expect this loss to be even smaller in actual observations where $N_{\rm s}$ will be much larger. The upper panels of Fig. 5 show the spherically averaged input model 21-cm brightness temperature power spectrum $P_{\rm T}(k)$ as a function of k. The figure also shows the binned input model power spectrum where we have considered $P_{\rm T}(k)$ at the $(k_\perp, k_{||})$ modes corresponding to the OWFA baselines and delay channels, and binned these into 20 equally spaced logarithmic bins.

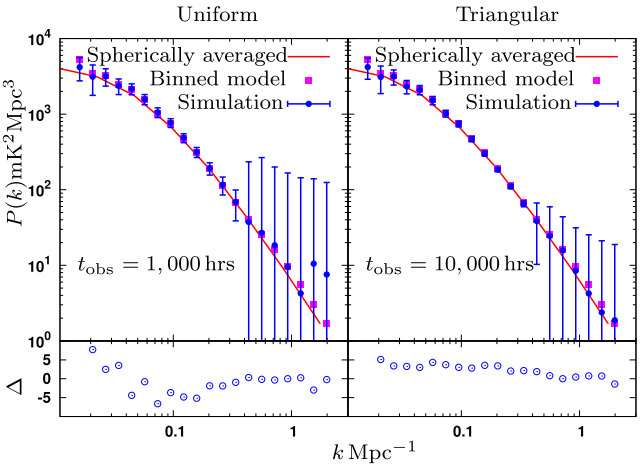

Figure 5. Considering the power spectrum, the upper panels show a comparison of the spherically averaged input model, the binned input model, and that estimated from the simulations. $N_{\rm r} = 1000$ statistically independent realizations of the simulation were used to estimate the mean and 1σ error bars shown here. The points in the bottom panels show Δ (equation 21), which quantifies the deviation between the binned input model and the simulated power spectrum.

The simulated H I 21-cm signal visbilities $\mathcal{S}\,(\boldsymbol{U}_a, \nu_n)$ considered here only contain the autocorrelation signal, as mentioned earlier the correlations between the adjacent baselines have not been incorporated here. We have used the simulated visibilities in equation (19) to estimate the power spectrum. The upper panels of Fig. 5 show the binned power spectrum $P(k)$ estimated from the simulations, the left- and the right panels show the results for uniform and triangular illuminations, respectively. The $N_{\rm r}$ realizations of the simulations were used to estimate the mean and the 1σ error bars shown in the figure. In both the cases, we find that the estimated power spectra are in good agreement with the input power spectrum. The error bars at the smallest k-bins are somewhat large due to the cosmic variance, though we see that a detection is possible here. At large k, the errors exceed the expected power spectrum, and a detection is not possible within the $t_{\rm obs}$ considered here. In both the illuminations, we see that the errors are relatively small in the k-range 0.05–0.3 Mpc^{-1}, which is most favourable for measuring the power spectrum with OWFA (Sarkar et al. 2017). The lower panels of Fig. 5 show the dimensionless ratio,

$$\Delta = \frac{\delta P(k)\,\sqrt{N_{\rm r}}}{\sigma} \,. \tag{21}$$

Here $N_{\rm r}$ is the number of realizations of the simulations, and $\delta P(k)$ is the difference between the estimated and the input model power spectrum. Ideally, we expect this to have a spread of the order of $\sigma/\sqrt{N_{\rm r}}$ around zero arising from statistical fluctuations. The normalized dimensionless ratio Δ is thus expected to have a variation of order unity provided the estimator provides an unbiased estimate of the power spectrum. We find that the values of Δ in the lower panels are distributed within ± 5 at all the bins except for that at the smallest k-value. The power spectrum is possibly underestimated at the lowest few baselines because the estimator ignores the convolution with the aperture power pattern that is included in the visibility signal (see equation 9 and also Choudhuri et al. 2014). This deviation is however seen to be well within the 1σ error bars for $t_{\rm obs} = 1000$ h of observation (upper left panel of 5). Overall, we conclude that

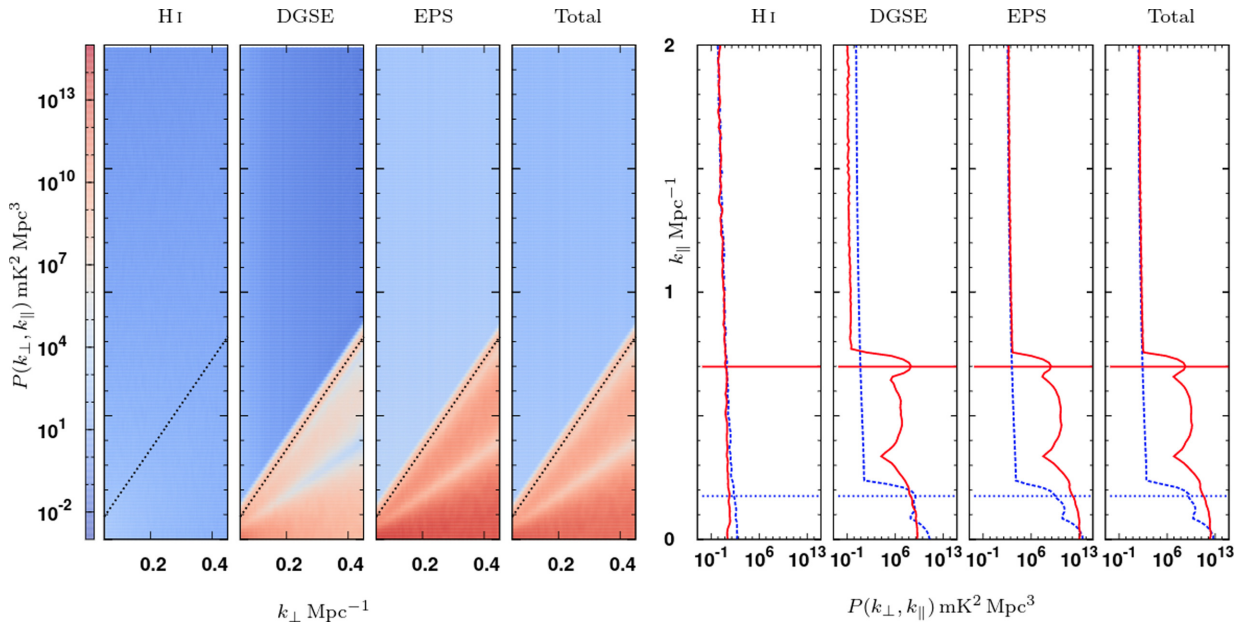

Figure 6. Predictions of the component-wise contributions to the 3DPS $P(k_\perp, k_\parallel)$ from the H I signal, the DGSE, the EPS, and the total 3DPS. The left panels show the cylindrical power spectrum $P(k_\perp, k_\parallel)$. The dotted lines mark the approximate wedge boundaries (equation 22). The right panels show vertical sections through the left panels for fixed $k_\perp = 0.095$ (in dashed lines) and $0.34\,\mathrm{Mpc}^{-1}$ (in solid lines). The horizontal solid lines and dotted lines in the right panels indicate the approximate wedge boundaries (equation 22) for the above mentioned $k_\perp$ modes.

our simulations validate the power spectrum estimator presented here.

5 RESULTS

We first focus on the H I signal and foreground predictions, and we have not included the noise contribution here. Considering the uniform illumination and the BN window function, the left panel of Fig. 6 shows the predicted cylindrical power spectrum $P(k_\perp, k_\parallel)$ averaged over 20 statistically independent realizations of the simulations for the H I signal, the individual DGSE and EPS foreground components and the total sky signal. We see that the foregrounds are largely confined within the 'Foreground Wedge' (Datta et al. 2010). The foreground contamination would be restricted to $k_\parallel = 0$ if the foregrounds were spectrally flat in the absence of the instrument, i.e. the visibilities $\mathcal{V}(\boldsymbol{U}, \nu)$ were independent of frequency. However, the fact that the baselines $U = d\,\nu/c$ change with frequency introduces a frequency dependence in $\mathcal{V}(\boldsymbol{U}, \nu)$ even if the sky signal is frequency independent. The foreground simulations here include both the ν scaling of U as well as the intrinsic ν dependence of the sky signal, and as a consequence the foreground contribution to $P(k_\perp, k_\parallel)$ extends out along $k_\parallel$ on to a wedge that is expected to be bounded by

$$k_\parallel = \left[\frac{r\,\sin(\theta_l)}{r'\,\nu_c}\right] k_\perp \tag{22}$$

in the $(k_\parallel, k_\perp)$ plane (Datta et al. 2010; Vedantham et al. 2012; Morales et al. 2012; Parsons et al. 2012; Trott et al. 2012), where θ_l refers to the largest angle (relative to the telescope's pointing direction) from which we have a significant foreground contamination. Here we consider $\theta_l = 90^\circ$ as the horizon limit. We see (Fig. 6) that there is a very large foreground contribution at $k_\parallel = 0$, and the foregrounds beyond this are largely contained within a wedge. The dotted line in the figure shows the wedge boundary predicted by equation (22): We see that the boundary of the simulated foreground wedge is located beyond the dotted line. The primary beam pattern $A(\Delta\boldsymbol{n}, \nu)$, the intrinsic frequency dependence of the sources introduced through the spectral index α and $F(\nu)$ all introduce additional frequency dependence (or chromaticity) in $\mathcal{V}(\boldsymbol{U}, \nu)$ that enhance the extent of the foreground wedge beyond that predicted by equation (22). We also notice that there are several structures visible inside the foreground wedge.

The right panels show vertical sections through the left panels, i.e. they show $P(k_\perp, k_\parallel)$ as a function of $k_\parallel$ for fixed $k_\perp$ values. We have chosen $k_\perp = 0.095$ and $0.34\,\mathrm{Mpc}^{-1}$ (dashed and solid lines, respectively) for which the horizontal lines show the corresponding wedge boundaries predicted by equation (22). Considering the foregrounds, the $k_\parallel$ dependence of $P(k_\perp, k_\parallel)$ shows two peaks, the first at $k_\parallel = 0$ and the second at the wedge boundary. The second peak corresponds to what is known as the 'pitch fork' effect (Thyagarajan et al. 2015; Thyagarajan et al. 2015), which is seen to be more prominent at the larger baseline. The foreground wedge is found to extend by $\Delta k_\parallel \simeq 0.1\,\mathrm{Mpc}^{-1}$ beyond the horizontal lines. In addition to this, we find oscillatory structures within the wedge where the $k_\parallel$ values of the dips correspond to the nulls in the primary beam pattern (i.e. replace θ_l in equation (22) with $\theta_1, \theta_2 \ldots$ the angular positions of the various nulls of the primary beam pattern). Considering large $k_\parallel$ beyond the wedge boundary, in all cases we find that $P(k_\perp, k_\parallel)$ drops to a small value that does not change very much with $k_\parallel$. This small value of $P(k_\perp, k_\parallel)$ arises due to the foreground leakage beyond the wedge. For DGSE, the value of $P(k_\perp, k_\parallel)$ decreases with increasing $k_\perp$. This reflects the fact that the DGSE contribution decreases with increasing ℓ ($\mathcal{C}_\ell \propto \ell^{-2.34}$). In contrast, the EPS contribution, which is Poisson dominated, does not change much with $k_\perp$.

Considering the H I signal (Fig. 6), we find that the foreground contribution is $\sim 10^{10}$ times larger at $k_\parallel = 0$ and other points within the wedge boundary. We also find that the foreground leakage remains $\sim 10^2$ times larger than the H I signal beyond the wedge boundary. This implies that the BN window is not a suitable choice for H I power spectrum detection with OWFA. Although the BN window function

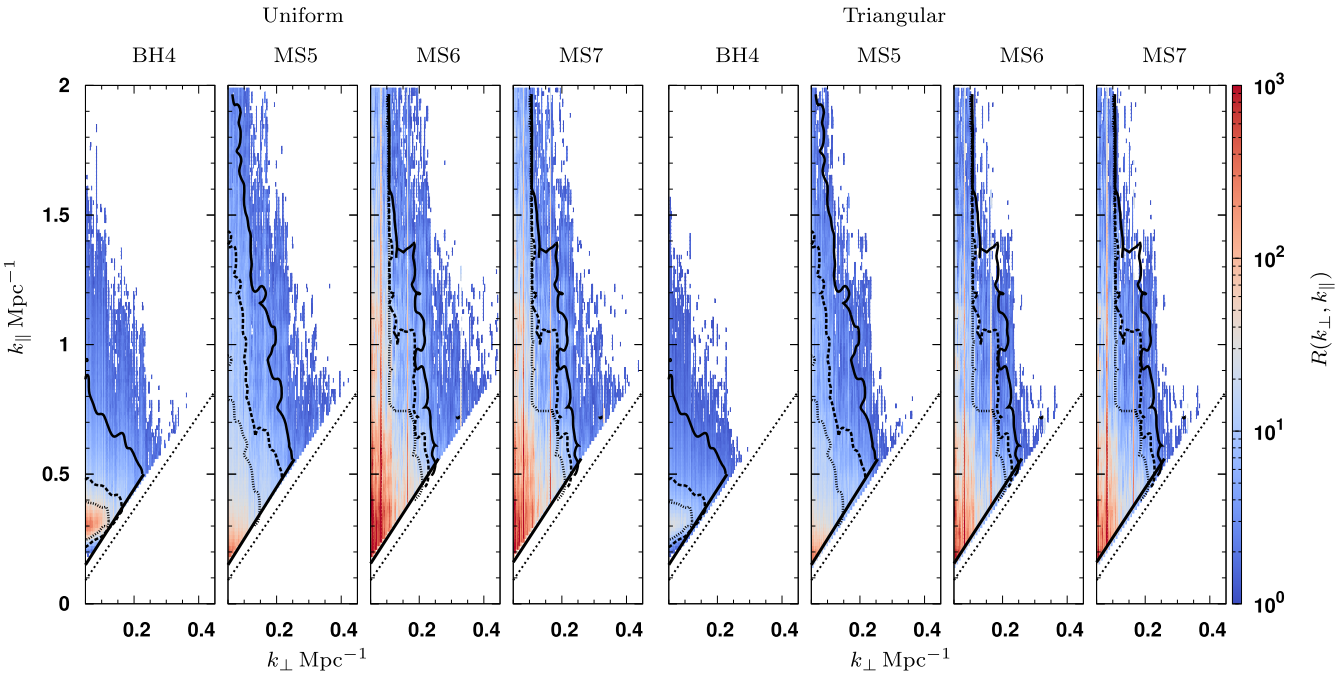

Figure 7. The ratio $R(k_\perp, k_\parallel)$ (equation 23) for different window functions considered in this work. The left- and right panels show the results for the uniform and triangular illumination, respectively. $R(k_\perp, k_\parallel) \geq 10, 50,$ and 100 regions for the triangular illumination are shown by the solid, dashed and fine-dotted contours, respectively, in both the left- and right panels. The triangular illumination considered here represents the worst possible scenario for the illumination pattern and the allowed $(k_\perp, k_\parallel)$ range for the actual OWFA beam pattern is not expected to be smaller than that of shown by the contours.

ensures that the values of the filtered visibilities are continuous at the boundary of the frequency band, discontinuities still persist in the various derivatives. The leakage in $P(k_\perp, k_\parallel)$ seen at large $k_\parallel$ beyond the wedge boundary arises from these discontinuities. Further, Fig. 6 shows an interesting feature that the leakage power $P(k_\perp, k_\parallel)$ appears to be proportional to $P(k_\perp, 0)$, which is the foreground power at $k_\parallel = 0$. We note that such a behaviour is not surprising as we expect the leakage amplitude to be proportional to the magnitude of the discontinuities that, in turn, are expected to be proportional to the overall foreground amplitude. Here $P(k_\perp, 0)$ provides a measure of the total foreground power (i.e. amplitude squared; equations 13 and 19).

In this paper, we consider the possibility of controlling the discontinuities at the band edges by suitably tailoring the window function. This leads us to investigate the possibility of using higher term window functions for H I power spectrum detection with OWFA. To this end, we make a comparative study of the expected foreground leakage for the set of window functions discussed earlier (equation 14 and Table 3).

To identify the $(k_\perp, k_\parallel)$ modes that can be used for the H I power spectrum detection, we introduce the ratio

$$R(k_\perp, k_\parallel) = P_{\rm T}(k_\perp, k_\parallel)/P_{\rm L}(k_\perp, k_\parallel)\,, \tag{23}$$

where $P_{\rm T}(k_\perp, k_\parallel)$ is the theoretically expected H I 21-cm signal power spectrum (equation 10) and $P_{\rm L}(k_\perp, k_\parallel)$ is the foreground leakage contribution. Fig. 7 shows $R(k_\perp, k_\parallel)$ for the different higher term window functions. The left- and right panels show the results for the uniform and the triangular illumination, respectively. We have only shown the points where $R(k_\perp, k_\parallel) > 1$, i.e. the H I signal exceeds the foreground leakage. For both the illumination patterns, we find that the largest values of $R(k_\perp, k_\parallel)$, which are in the range 50–500, are located at the lowest $(k_\perp, k_\parallel)$ modes just beyond the wedge boundary. The values of $R(k_\perp, k_\parallel)$ and the region where $R(k_\perp, k_\parallel) > 1$ both increase as we increase the number of terms in the window function. In all cases, we have $R(k_\perp, k_\parallel) < 1$ at large $(k_\perp, k_\parallel)$ where the H I signal is small. In comparison to the uniform illumination, the region where $R(k_\perp, k_\parallel) > 1$ is found to be somewhat smaller for the triangular illumination because of the larger FoV.

We have assumed that the $(k_\perp, k_\parallel)$ region where $R(k_\perp, k_\parallel) \geq R_{\rm t}$ can be used to detect the H I 21-cm signal power spectrum. $R_{\rm t}$ here is a threshold value that has to be set sufficiently high so as to minimize the possibility of residual foreground contamination. We discuss the criteria for deciding the value of $R_{\rm t}$ later in this section. We see that the $(k_\perp, k_\parallel)$ region corresponding to different values of $R_{\rm t}$ are somewhat smaller for the triangular illumination as compared to the uniform illumination. The OWFA illumination pattern is unknown, but we expect the actual OWFA predictions to be somewhere between the uniform and the triangular predictions. The $(k_\perp, k_\parallel)$ range that simultaneously satisfies $R(k_\perp, k_\parallel) \geq R_{\rm t}$ for both the uniform and the triangular illuminations can safely be used to detect the H I 21-cm signal power spectrum. The $R(k_\perp, k_\parallel) \geq R_{\rm t}$ regions for $R_{\rm t} = 10,\ 50,$ and 100 for the triangular illumination are shown by the solid, dashed, and fine-dotted contours respectively in both the left- and right panels. The triangular illumination considered here represents the worst possible scenario for the illumination pattern of the OWFA antennas. We do not expect the allowed $(k_\perp, k_\parallel)$ range for the actual OWFA beam pattern to be smaller than that predicted for the triangular illumination. Thus, for any value of $R_{\rm t}$, throughout we have used the triangular illumination to determine the allowed $(k_\perp, k_\parallel)$ range.

From Fig. 7, we see that the allowed $(k_\perp, k_\parallel)$ region and the peak $R(k_\perp, k_\parallel)$ values increase as we increase the number of terms in the window function. It thus appears to be advantageous for H I 21-cm signal detection to increase the number of terms in the window function. This would indeed be true if the power spectrum estimated at the different $(k_\perp, k_\parallel)$ modes were uncorrelated. However, the

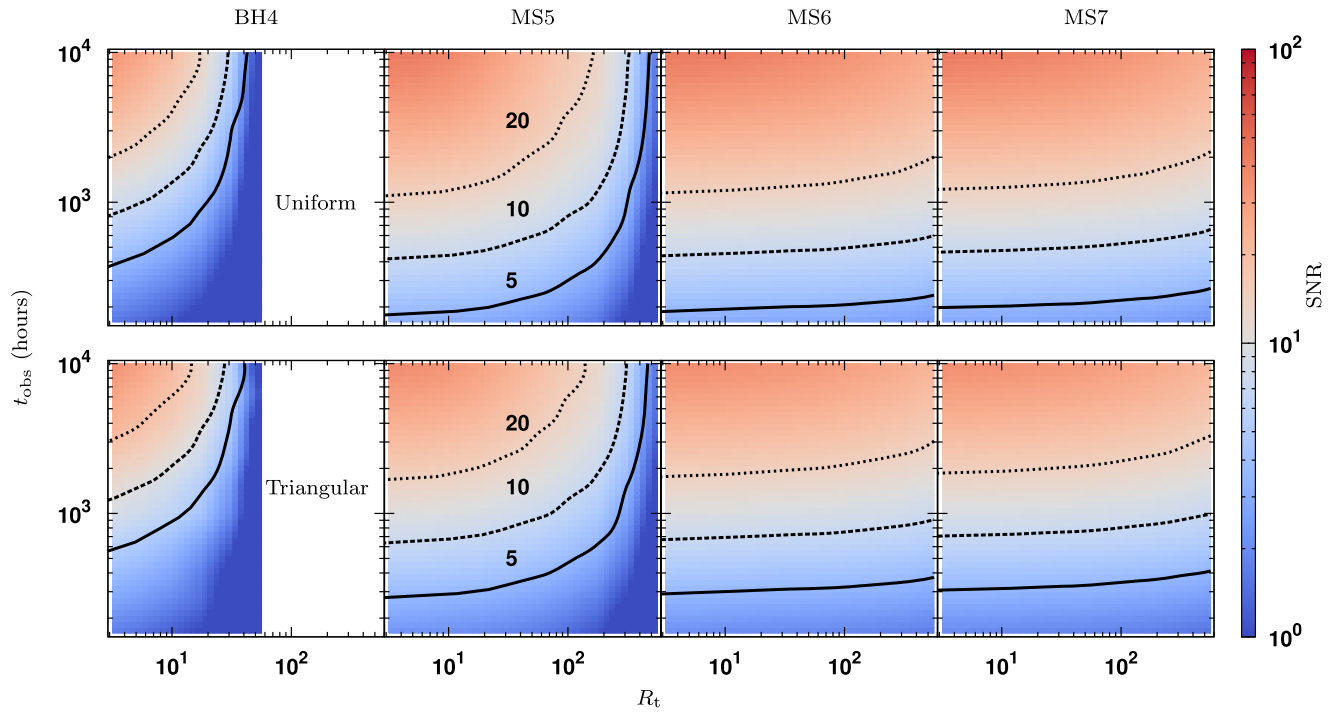

Figure 8. A comparison of predicted SNRs for different higher term window functions considered in this work. The upper and lower panels show the predictions for the uniform and triangular illuminations, respectively. The SNR values 5, 10, and 20 are shown by the solid, dashed, and dotted contours, respectively.

convolution in equation (15) causes the H I signal at different $k_{\shortparallel}$ modes to be correlated. We see that $\tilde{f}(\tau_m)$ gets wider (right panel of Fig. 4), causing the $k_{\shortparallel}$ extent of the correlations to increase as we increase the number of terms in the window function. The system noise contribution at the different $k_{\shortparallel}$ modes are also expected to be correlated because of the convolution. Further, the window function $F(\nu)$ gets narrower (left panel of Fig. 4) and the loss in the H I signal at the edge of the frequency band also increases as we increase the number of terms. It is therefore not obvious whether it is advantageous for H I 21-cm signal detection to increase the number of terms in the window function. Rather, it would be more appropriate to ask as to which of the different window functions considered here is best suited for H I signal detection. In order to quantitatively address this issue, we consider a figure of merit namely the SNR for measuring $A_{\rm HI} = b_{\rm HI}^2\,\bar{x}_{\rm HI}^2$, which is the amplitude of the H I 21-cm signal power spectrum (equation 10). We have used the Fisher-matrix formalism where the SNR for the measurement of $A_{\rm HI}$ is given by

$$\mathrm{SNR}^2 = \sum_{a,m,m'} \frac{\partial P_{\rm T}(k_{\perp a}, k_{\parallel m})}{\partial \ln A_{\rm HI}} \boldsymbol{C}_a^{-1}(m,m') \frac{\partial P_{\rm T}(k_{\perp a}, k_{\parallel m'})}{\partial \ln A_{\rm HI}} \,. \tag{24}$$

Here we have assumed that the entire allowed ($k_\perp$, $k_{\shortparallel}$) range where $R(k_\perp, k_{\shortparallel}) \geq R_{\rm t}$ is combined to estimate $A_{\rm HI}$. Considering $\Delta\hat{P}\,(\boldsymbol{U}_a, \tau_m) = \hat{P}\,(\boldsymbol{U}_a, \tau_m) - P\,(\boldsymbol{U}_a, \tau_m)$, the error in estimated the 21-cm power spectrum, the correlation between different $k_{\shortparallel}$ mode arising from the convolution in equation (15) can be quantified through the covariance matrix ,

$$\boldsymbol{C}_a(m,m') = \langle [\Delta\hat{P}\,(\boldsymbol{U}_a, \tau_m)][\Delta\hat{P}\,(\boldsymbol{U}_a, \tau_{m'})] \rangle \,. \tag{25}$$

We have estimated $P\,(\boldsymbol{U}_a, \tau_m)$ and $\boldsymbol{C}_a(m,m')$ for different window functions and different values of $t_{\rm obs}$ using simulations. For each case, we have used $N_{\rm r} = 1000$ statistically independent realizations of the OWFA visibilities incorporating the H I signal and the system noise.

Fig. 8 shows the predicted SNR values as a function of $t_{\rm obs}$ and $R_{\rm t}$. The four columns, respectively, correspond to the four higher term window functions, whereas the two rows respectively correspond to the uniform and triangular illuminations. Our aim here is to identify the optimal window function. Considering BH4, we find that the SNR values are considerably lower compared to the three other window functions and BH4 is not a good choice. We find that for the entire $R_{\rm t}$ range considered here ($1 \leq R_{\rm t} \leq 500$), the SNR values do not differ much between the MS6 and MS7 window functions. The SNR values for the MS5 window function also are comparable to those for MS6 and MS7 for $R_{\rm t} \lesssim 30$; however, the SNR values for MS5 drop rapidly for larger $R_{\rm t} (> 30)$. Fig. 8 therefore indicates that BH4 can definitely be excluded; however, all three MS5, MS6, and MS7 exhibit comparable performance if one wishes to use a threshold $R_{\rm t} < 30$. For a higher threshold $R_{\rm t} > 30$, MS5 also is excluded; however, both MS6 and MS7 exhibit comparable performance.

In order to quantify the small differences in the SNR predictions of the window functions, we consider the ratio of the SNRs for the different window functions with respect to that for MS6 that we take as reference :

$$\mathcal{R}(R_{\rm t}, t_{\rm obs}) = \mathrm{SNR}(R_{\rm t}, t_{\rm obs}) / [\mathrm{SNR}(R_{\rm t}, t_{\rm obs})]_{\rm MS6} \,. \tag{26}$$

A value $\mathcal{R}(R_{\rm t}, t_{\rm obs}) > 1$ tells us that the corresponding window function performs better than MS6, whereas the converse is true if $\mathcal{R}(R_{\rm t}, t_{\rm obs}) < 1$. The left-, middle, and right panels of Fig. 9 show $\mathcal{R}(R_{\rm t}, t_{\rm obs})$ as a function of $t_{\rm obs}$ for $R_{\rm t} = 10,\ 50,$ and 100, respectively. As expected, the $\mathcal{R}(R_{\rm t}, t_{\rm obs})$ values always remain substantially below 1.0 for BH4 and this is excluded. Note that the $\mathcal{R}(R_{\rm t}, t_{\rm obs})$ values for BH4 are not visible in the middle and right panels due to the very small allowed $(k_\perp, k_{\shortparallel})$ region at these $R_{\rm t}$ values. Considering MS5 next, for $R_{\rm t} = 10$, we find that $\mathcal{R}(R_{\rm t}, t_{\rm obs}) \geq 1.0$,

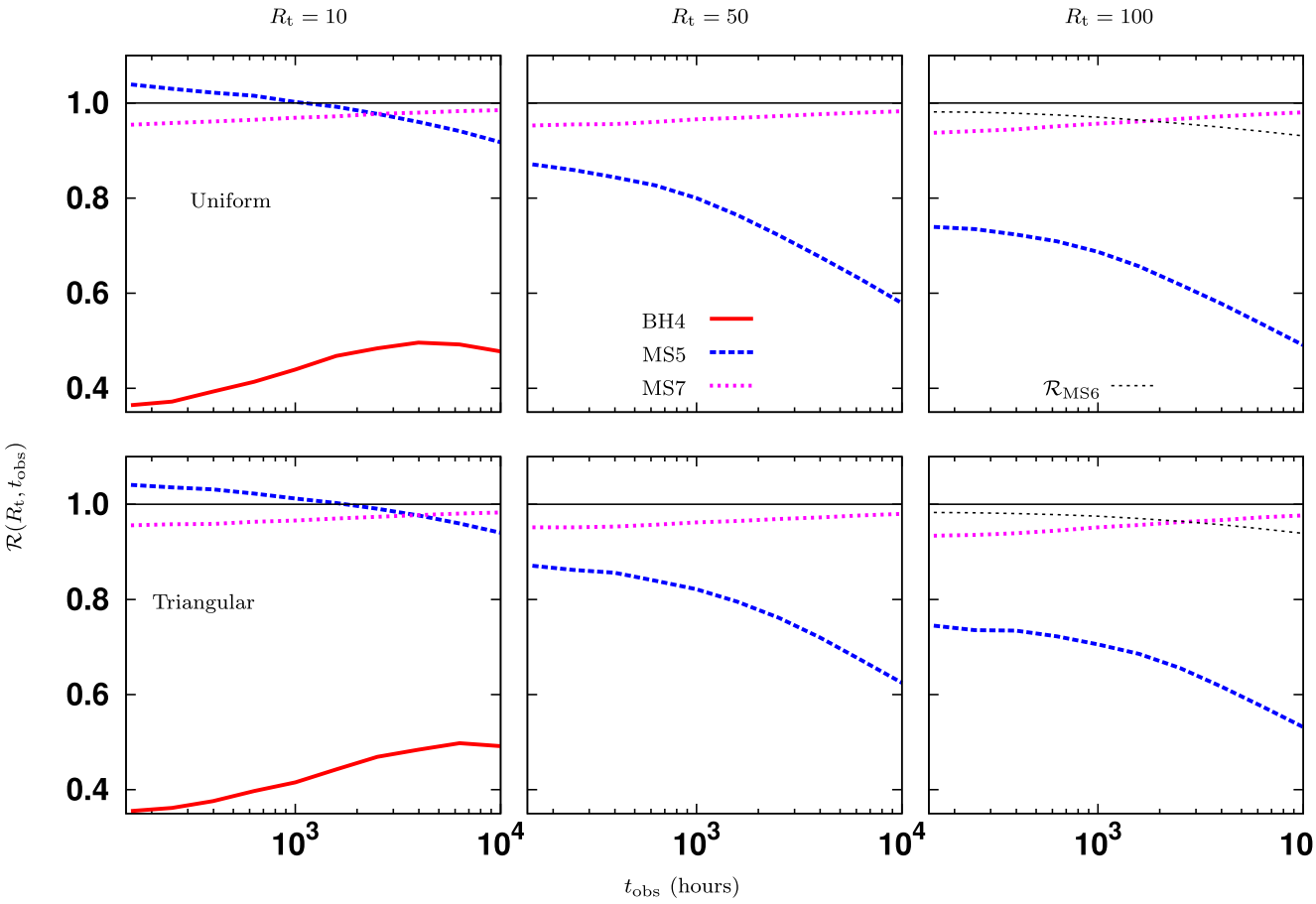

Figure 9. A comparison of $\mathcal{R}(R_t, t_{obs})$ for different window functions considered in this work. The upper and lower panels show the predictions for the uniform and triangular illuminations, respectively. The left, middle, and right panels show the results for the three cases where $R_t = 10,\ 50,$ and 100, respectively. The thin dashed line in the right panels shows the ratio $\mathcal{R}_{MS6} = [\mathrm{SNR}(R_t = 100, t_{obs})]_{MS6}/[\mathrm{SNR}(R_t = 50, t_{obs})]_{MS6}$.

provided $t_{obs} \leq 1000$ h; however, $\mathcal{R}(R_t, t_{obs}) < 1$ if $t_{obs} > 1000$ h and it declines steadily with increasing t_{obs}. For $R_t = 50$ and 100, we have $\mathcal{R}(R_t, t_{obs}) < 1$ irrespective of t_{obs}. Considering MS7, we find that $0.9 < \mathcal{R}(R_t, t_{obs}) < 1.0$ for all the three R_t values shown here. This is a direct consequence of the fact that the extent of the correlation between the $k_{\shortparallel}$ modes increases (Fig. 4) with an increase in the number of terms in the window function. Although the allowed ($k_\perp$, $k_{\shortparallel}$) region increases if we increase the number of terms, the enhanced correlation causes the SNR to degrade beyond MS6. The uniform and triangular illuminations both show very similar results. Our analysis suggests that the MS5 window is optimal at small R_t (e.g. $R_t \leq 30$) and small t_{obs} (e.g. $t_{obs} \leq 1000$ h); barring this situation, the MS6 window function is optimal for H I power spectrum estimation with OWFA.

Once we have identified the optimal window function, we next aim to fix a suitable R_t for H I 21-cm power spectrum estimation. We have earlier discussed that the value of R_t must be set sufficiently high to minimize the possibility of residual foreground contamination. Shorter observations (e.g. $t_{obs} \leq 1000$ h) are expected to have a relatively large noise contribution, and it is possibly adequate to consider a less conservative threshold $R_t \approx 10$ along with the MS5 window function for H I power spectrum estimation. For $t_{obs} \geq 1000$ h, where we target a more precise measurement of the H I power spectrum, it is worth considering a more conservative threshold $R_t \geq 50$ and use the MS6 window function. The question is whether the SNR would fall significantly if we increase the value of the threshold R_t in the range 50–100. The thin dashed line in the right panels of Fig. 9 shows the ratio $\mathcal{R}_{MS6} = [\mathrm{SNR}(R_t = 100, t_{obs})]_{MS6}/[\mathrm{SNR}(R_t = 50, t_{obs})]_{MS6}$. We find that the SNR values degrade at most by ~ 8 per cent if we increase R_t from 50 to 100. This indicates that one can set the value of the threshold R_t as high as 100 without a significant loss of SNR. For $R_t = 100$, the residual foreground contamination is expected to be ≤ 1 per cent for every ($k_\perp$, $k_{\shortparallel}$) modes that is used for H I power spectrum estimation .

An earlier study (Sarkar et al. 2017) has predicted that a 5σ detection of the binned power spectrum is possible in the $k = \sqrt{k_\perp^2 + k_\parallel^2}$ range $0.05 \leq k \leq 0.3\,\mathrm{Mpc}^{-1}$ with 1000 h of observation; this, however uses the entire available ($k_\perp$, $k_{\shortparallel}$) region and does not take the foreground contamination into account. The fact is that a significant ($k_\perp$, $k_{\shortparallel}$) range has to be excluded due to the foreground wedge and the residual foreground leakage. We next consider the revised SNR predictions for the binned H I power spectrum taking into account the ($k_\perp$, $k_{\shortparallel}$) modes that have to be excluded to avoid the foreground contamination. For these predictions, we have used the MS6 window function and set a high threshold of $R_t = 100$; the results do not change very much if R_t is varied in the range $R_t = 10$ and 100 (Fig. 8). The range $k \leq 0.1\,\mathrm{Mpc}^{-1}$ is completely within the foreground wedge, and this is excluded from H I power spectrum estimation. We have binned the allowed k-range ($0.1 < k < 2.0\,\mathrm{Mpc}^{-1}$) into 10 logarithmic bins and estimated the

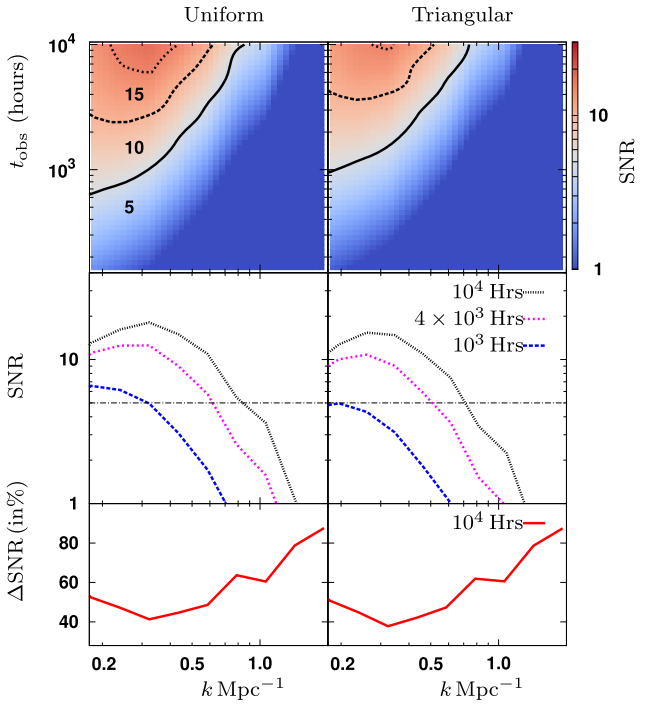

Figure 10. The SNR predictions for the binned power spectrum estimation using MS6 window function for the triangular and uniform illuminations. Here we have set $R_t = 100$. The upper panels show the predicted SNR as a function of k and t_{obs}. The contours mark the SNR values 5, 10, and 15 (mentioned in the figure). The middle panels show horizontal sections through the upper panels for $t_{obs} = 1000$, 4000, and 10^4 h (mentioned in the figure legend). The horizontal dot–dashed line marks the SNR value 5. The lower panels show the percentage loss of SNR (ΔSNR) due to the presence of the foregrounds for $t_{obs} = 10^4$ h.

SNR prediction for different t_{obs}. The upper row of Fig. 10 shows the SNR predictions as a function of k and t_{obs}, with the left- and right panels corresponding to the uniform and triangular illuminations, respectively. The middle row shows horizontal sections through the upper panels, i.e. they show the SNR as a function of k for fixed values of t_{obs} (mentioned in the figure legend), and the lower row shows the percentage loss of SNR (ΔSNR) due to the excluded ($k_\perp$, $k_{\shortparallel}$) region. To calculate ΔSNR, we have used the SNR predictions considering the entire available ($k_\perp$, $k_{\shortparallel}$) region (similar to Sarkar et al. 2017) as reference.

Considering the upper row of Fig. 10, we see that the SNR predictions are similar for both the illuminations but the SNR values are ∼1.5 times lower for the triangular illumination in comparison to the uniform illumination. Our results are also similar to those in fig. 3 of Sarkar et al. (2017) except that our prediction for the uniform illumination is ∼1.5 times lower due to the foreground contamination. We find that at low t_{obs}, the SNR peaks in the smallest k-bin (~ 0.18Mpc^{-1}) and a $5\,\sigma$ measurement is possible at this k-bin with $t_{obs} \approx 600$ and 1000 h for the uniform and triangular illuminations, respectively. A $5\,\sigma$ detection of the binned power spectrum is possible in the k-range $0.18 \leq k \leq 0.3$ Mpc^{-1} with $t_{obs} \sim$ 1000 h for the uniform illumination, whereas this will require $t_{obs} \sim$ 2000 h for the triangular illumination. The peak SNR shifts towards larger k-bins for larger t_{obs}, and the peak is at $k \sim 0.3$ Mpc^{-1} for $t_{obs} = 10^4$ h, where a $15\,\sigma$ detection is possible. The shift in the peak SNR is clearly visible in the middle row of the figure. A $10\,\sigma$ detection is possible in the range $k \sim 0.2$–0.4 Mpc^{-1} with $t_{obs} \sim 3000$ and 4000 h for the uniform and triangular illuminations, respectively. The SNR falls drastically at large k (> 0.8 Mpc^{-1}); this is also noticeable in fig. 3 of Sarkar et al. (2017) and this is due to the fact that the H I power spectrum fall at large k (Fig. 5) whereby these bins are dominated by the system noise contribution. The situation is further aggravated here because a considerable fraction of the available ($k_\perp$, $k_{\shortparallel}$) region has to be excluded to avoid the foregrounds. Considering the lower row of the figure, we see that the fractional loss in the SNR (ΔSNR) is > 60 per cent at $k > 0.8$ Mpc^{-1}, and it increases rapidly to ~ 80 per cent at the larger k-bins. The fractional loss in the SNR is in the range 40–60 per cent for k in the range $0.18 \leq k \leq 0.8$ Mpc^{-1}, where there are prospects of a detection. We also note that (ΔSNR) is minimum at $\lesssim 40$ per cent at $k \sim 0.3$ Mpc^{-1} where the SNR peaks for $t_{obs} \geq 10^4$ h.

6 SUMMARY AND CONCLUSION

The ORT (Swarup et al. 1971) is currently being upgraded to operate as a radio interferometer, the OWFA (Subrahmanya et al. 2017b), and this work focuses on PII of OWFA. The array operates with a single linear polarization. The ORT (and also OWFA) feed system consists of linear dipoles arranged end to end along the long axis of the cylindrical parabolic reflector. Considering any particular dipole, its radiation pattern is minimum along the direction of the adjacent dipoles and we thus expect minimal coupling between the adjacent dipoles. The actual primary beam patten $A(\Delta\hat{\boldsymbol{n}}, \nu)$ for OWFA is unknown. For this study, we use two extreme models for $A(\Delta\hat{\boldsymbol{n}}, \nu)$: The first one is based on the simplest assumption that the OWFA antenna aperture is uniformly illuminated by the dipole feeds (uniform illumination), whereas the second one assumes a triangular illumination pattern (Fig. 3). We expect the actual OWFA illumination to be somewhat in between these two scenarios.

OWFA is sensitive to the HI 21-cm signal from $z = 3.35$, and measuring the cosmological 21-cm power spectrum is one of the main goals of this upcoming instrument. The cosmological H I 21-cm signal is faint and is buried in foregrounds that are several orders of magnitude brighter. The foregrounds processed through the chromatic response of the instrument produce spectral features that contaminate the H I signal, and this poses a severe challenge for detecting the 21-cm power spectrum. In this paper, we have simulated the H I 21-cm signal and foregrounds expected for OWFA PII. Our aim here is to use these simulations to quantify the extent of the expected foreground contamination and asses the prospects of detecting the 21-cm power spectrum.

We have used all-sky foreground simulations (described in Section 2) that incorporate the contributions from the two most dominant components namely the diffuse Galactic synchrotron emission and the extragalactic point sources. These were used to calculate the foreground contribution $\mathcal{F}(\boldsymbol{U}_a, \nu_n)$ to the model visibilities (equation 5) expected at OWFA. These simulations incorporate the chromatic behaviour of both the sources and also the instrument. To simulate the H I signal contribution to the model visibilities $\mathcal{S}(\boldsymbol{U}_a, \nu_n)$ (equation 8), we use the 'Simplified Analysis' presented in Sarkar et al. (2018a). This is based on the flat-sky approximation, and also ignores the correlation between the H I signal at adjacent baselines and the non-ergodic nature of the H I visibility signal along the frequency axis. To estimate the 21-cm power spectrum from the measured visibilities, we introduce an estimator (equation 19) that has been constructed so as to eliminate the noise bias and provide an unbiased estimate of the 3D power spectrum $P(k_\perp, k_{\shortparallel})$. We have validated this for both the uniform and the triangular illuminations

using a large number of statistically independent realizations of H I simulations. These particular simulations also include the system noise; the foregrounds however are ignored. We find (Fig. 5) that in the absence of foregrounds, for both the illuminations, the k-range 0.05–0.3 Mpc^{-1} is most favourable for measuring the power spectrum with OWFA. This is consistent with the results of earlier work (Sarkar et al. 2017).

Considering the foregrounds, the contamination is primarily localized within a wedge shaped region of the $(k_\perp, k_{\shortparallel})$ plane (Fig. 6). The k modes outside this 'foreground wedge' are believed to be largely uncontaminated by the foregrounds. However, there is a relatively small fraction of the foreground that leaks out beyond the wedge. Though small, this foreground leakage may still exceed the expected H I signal in many of the k modes outside the foreground wedge. For signal detection, we focus on a strategy referred to as 'foreground avoidance' where only the k modes that are expected to be uncontaminated are used for measuring the 21-cm power spectrum. In this work, we use simulations to identify the region of the $(k_\perp, k_{\shortparallel})$ plane that is expected to be uncontaminated, and we use this to quantify the prospects of measuring the 21-cm power spectrum using OWFA.

Our simulations show that foreground leakage outside the wedge, though small, can still exceed the 21-cm power spectrum expected at OWFA. We find that the extent of foreground leakage is extremely sensitive to the frequency window function $F(\nu)$ (equation 13) that is introduced (Vedantham et al. 2012) to suppress the measured visibilities near the boundaries of the frequency band. Considering the extensively used (e.g. Paul et al. 2016) BN filter that has four terms, we find that the foreground leakage exceeds the expected 21-cm power spectrum at all the available k modes, and it will not be possible to measure the 21-cm power spectrum using OWFA. In order to overcome this problem, we consider a set of cosine window functions with progressively increasing number of terms (Table 3 and Fig. 4). The window function gets narrower resulting in better suppression at the edges of the band as we increase the number of terms. Using $R(k_\perp, k_{\shortparallel})$, which is the ratio of the expected 21-cm power spectrum to the foreground leakage contribution, we find that the $(k_\perp, k_{\shortparallel})$ region where $R(k_\perp, k_{\shortparallel}) > 1$ (i.e. the region where H I signal exceeds the foreground leakage) increases if we increase the number of terms in the window function (Fig. 7). Taken at face value, this indicates that it is advantageous to increase the number of terms in the window function. It is however also necessary to take into consideration the fact that the H I signal in adjacent $k_{\shortparallel}$ modes get correlated due to $F(\nu)$ and the extent of this correlation increases as we increases the number of terms. The number of independent estimates of the 21-cm power spectrum thus gets reduced if we increase the number of terms. We therefore need to choose the optimal window function by balancing between these two competing effects. We have used the Fisher matrix formalism to define the SNR (equation 24) for measuring the amplitude of the 21-cm power spectrum, and we use this as a figure of merit to identify the optimal window function.

Our analysis (Fig. 8) shows that the optimal choice of window function depends on the observing time $t_{\rm obs}$ and the threshold value $R_{\rm t}$. A threshold value $R_{\rm t}$ implies that we only use the modes where $R(k_\perp, k_{\shortparallel}) \geq R_{\rm t}$ for measuring the 21-cm power spectrum. We note that the value of $R_{\rm t}$ must be set sufficiently high to minimize the possibility of residual foreground contamination. We find that the five-term MS5 window function is optimal at small $t_{\rm obs}$ ($\leq$1000 h) and small $R_{\rm t}$ ($\leq$30), whereas the six-term MS6 window function is optimal for larger values of $t_{\rm obs}$ and $R_{\rm t}$. Relative to MS6, the SNR is found to degrade slightly if we consider the seven term MS7 window function. The uniform and triangular illuminations both show very similar results.

We propose a possible observational strategy based on the finding summarized above. Shorter observations (e.g. $t_{\rm obs} \leq 1000$ h) are expected to have a relatively large noise contribution, and it is possibly adequate to consider a relatively low threshold $R_{\rm t} \approx 10$ along with the MS5 window function. For longer observations, $t_{\rm obs} \geq 1000$ h, where we target a more precise measurement of the 21-cm power spectrum, it is worth considering a more conservative threshold $R_{\rm t} \geq 50$ and use the MS6 window function. Our investigations also show that the SNR does not fall much if $R_{\rm t}$ is increased from 50 to 100, and we could equally well consider using a very conservative threshold of $R_{\rm t} = 100$ where the contribution from foreground leakage is expected to be less than 1 per cent of the 21-cm power spectrum.

The SNR values for measuring the amplitude of the 21-cm power spectrum (Fig. 8) are approximately 1.5 times lower for the triangular illumination in comparison to the uniform Illumination. Using MS5 with $R_{\rm t} \approx 30$, a 5σ detection will take $\sim$180 and $\sim$300 h with the uniform and triangular illuminations, respectively. The same is increased to $\sim$200 and $\sim$300 h if we use MS6 or MS7 with $R_{\rm t} \approx 100$.

We have also considered the prospects of measuring the binned 21-cm power spectrum. The discussion here is restricted to MS6 with $R_{\rm t} = 100$. We find that the range $k \leq 0.1\ \mathrm{Mpc}^{-1}$ is completely within the foreground wedge (Fig. 10) and has to be excluded. For low $t_{\rm obs}$, the SNR peaks at the smallest $k \approx 0.18\mathrm{Mpc}^{-1}$ bin and a $5\,\sigma$ measurement is possible at this k-bin with $t_{\rm obs} \approx 600$ and 1000 h for the uniform and triangular illuminations, respectively. A $5\,\sigma$ detection of the binned power spectrum is possible in the k-range $0.18 \leq k \leq 0.3\ \mathrm{Mpc}^{-1}$ with $t_{\rm obs} \sim 1000$ h for the uniform illumination, whereas this will require $t_{\rm obs} \sim 2000$ h for the triangular illumination. Considering $t_{\rm obs} = 10^4$ h, for both the illuminations, the peak SNR shifts to larger k-values 0.3–0.4 Mpc^{-1} and a $5\,\sigma$ detection is possible in the range $0.18 \leq k \leq 0.8\ \mathrm{Mpc}^{-1}$. We have used ΔSNR to quantify the fractional loss in SNR due to the foreground contamination; the comparison here is with respect to the situation where there are no foregrounds. We find that ΔSNR has values in the range 40–60 per cent for k in the range $0.18 \leq k \leq 0.8\ \mathrm{Mpc}^{-1}$, where there are good prospects of measuring the 21-cm power spectrum.

The exact beam pattern of OWFA is not known, but we expect this to be somewhere between the uniform and triangular illuminations considered here. We therefore expect the actual situation for measuring the 21-cm power spectrum to lie somewhere between the two different sets of predictions presented here. This study indicates that 'Foreground Avoidance' provides an effective technique for measuring the 21-cm power spectrum with OWFA. It is also predicted that a $5\,\sigma$ measurement of the 21-cm power spectrum should be possible within approximately a few hundred hours of observations despite the k modes that have to be excluded due to foreground contamination. It is however necessary to note that the entire analysis presented here is based on 20 statistically independent realizations of our specific foreground model. While this model attempts to incorporate the salient features of the two dominant foreground components, it still remains to establish how robust the results are with respect to variations in the foreground model. Although the exact quantum of foreground leakage may vary depending on the foreground model, we do not expect this to be a very severe effect as we have adopted a pretty conservative threshold $R_{\rm t} = 100$ for a considerable part of our analysis. Calibration (Marthi & Chengalur 2014) is another issue that could affect the results presented here. In future work, we plan to study the effect of calibration errors and also the effect of varying the foreground model.

ACKNOWLEDGEMENTS

The authors would like to thank Jayaram N. Chengalur for useful suggestions and discussions. SC acknowledges the University Grant Commission, India, for providing financial support through Senior Research Fellowship. SC would also like to thank Abinash Kumar Shaw for helpful discussions and suggestions. VRM acknowledges support of the Department of Atomic Energy, Government of India, under project no. 12-R&D-TFR-5.02-0700.

DATA AVAILABILITY

The data underlying this paper will be shared on reasonable request to the corresponding author.

REFERENCES

Albrecht H. H., 2001, IEEE International Conference on Acoustics, Speech, and Signal Processing, Proceedings (Cat. No.01CH37221), 5, p. 3081
Ali S. S., Bharadwaj S., 2014, J. Astrophys. Astron., 35, 157
Ali S. S., Bharadwaj S., Pandey B., 2005, MNRAS, 363, 251
Ali S. S., Bharadwaj S., Chengalur J. N., 2008, MNRAS, 385, 2166
Bandura K. et al., 2014, in Takahashi T., deh Herder J.-W. A., Bautz M., eds, Proc. SPIE Conf. Ser. Vol. 9145, Ground-based and Airborne Telescopes V. SPIE, Bellingham, p. 914522
Berger P., et al., 2016, in Hall H. J., Gilmozzi R., Marshall H. K., eds, Proc. SPIE Conf. Ser. Vol. 9906, Ground-based and Airborne Telescopes VI. SPIE, Bellingham, p. 99060D
Bernardi G. et al., 2009, A&A, 500, 965
Bharadwaj S., Ali S. S., 2005, MNRAS, 356, 1519
Bharadwaj S., Pandey S. K., 2003, J. Astrophys. Astron., 24, 23
Bharadwaj S., Sethi S. K., 2001, J. Astrophys. Astron., 22, 293
Bharadwaj S., Nath B. B., Sethi S. K., 2001, J. Astrophys. Astron., 22, 21
Bharadwaj S., Sethi S. K., Saini T. D., 2009, Phys. Rev. D, 79, 083538
Bharadwaj S., Sarkar A. K., Ali S. S., 2015, J. Astrophys. Astron., 36, 385
Biggs A. D., Ivison R. J., 2006, MNRAS, 371, 963
Blake C., Ferreira P. G., Borrill J., 2004, MNRAS, 351, 923
Bull P., Ferreira P. G., Patel P., Santos M. G., 2015, ApJ, 803, 21
Castorina E., Villaescusa-Navarro F., 2017, MNRAS, 471, 1788
Chang T.-C., Pen U.-L., Peterson J. B., McDonald P., 2008, Phys. Rev. Lett., 100, 091303
Chang T.-C., Pen U.-L., Bandura K., Peterson J. B., 2010, Nature, 466, 463
Chatterjee S., Bharadwaj S., 2018a, MNRAS, 483, 2269
Chatterjee S., Bharadwaj S., 2018b, MNRAS, 478, 2915
Chen X., 2012, Int. J. Mod. Phys. Conf. Ser., 12, 256
Chen X., 2015, IAU Gen. Assem., 22, 2252187
Choudhuri S., Bharadwaj S., Ghosh A., Ali S. S., 2014, MNRAS, 445, 4351
Choudhuri S., Bharadwaj S., Chatterjee S., Ali S. S., Roy N., Ghosh A., 2016, MNRAS, 463, 4093
Choudhuri S., Bharadwaj S., Ali S. S., Roy N., Intema H. T., Ghosh A., 2017, MNRAS, 470, L11
Datta A., Bowman J. D., Carilli C. L., 2010, ApJ, 724, 526
De Oliveira-Costa A., Tegmark M., Gaensler B. M., Jonas J., Landecker T. L., Reich P., 2008, MNRAS, 388, 247
Eastwood M. W. et al., 2019, American Astronomical Society, 158, 84
Eisenstein D. J., Hu W., 1999, ApJ, 511, 5
Ghosh A., Bharadwaj S., Ali S. S., Chengalur J. N., 2011a, MNRAS, 411, 2426
Ghosh A., Bharadwaj S., Ali S. S., Chengalur J. N., 2011b, MNRAS, 418, 2584
Ghosh A., Prasad J., Bharadwaj S., Ali S. S., Chengalur J. N., 2012, MNRAS, 426, 3295
Ginzburg V. L., Syrovatskii S. I., 1969, ARA&A, 7, 375
Górski K. M., Hivon E., Banday A. J., Wandelt B. D., Hansen F. K., Reinecke M., Bartelmann M., 2005, ApJ, 622, 759
Harris F. J., 1978, Proc. IEEE, 66, 51
Hazra D. K., Sarkar T. G., 2012, Phys. Rev. Lett., 109, 121301
Iacobelli M. et al., 2013, A&A, 558, A72
Kogut A., Banday A. J., Bennett C. L., Gorski K. M., Hinshaw G., Reach W. T., 1996, ApJ, 460, 1
La Porta L., Burigana C., Reich W., Reich P., 2008, A&A, 479, 641
Marthi V. R., 2017, J. Astrophys. Astron., 38, 12
Marthi V. R., Chengalur J., 2014, MNRAS, 437, 524
Marthi V. R., Chatterjee S., Chengalur J. N., Bharadwaj S., 2017, MNRAS, 471, 3112 (Paper I)
Masui K. W., McDonald P., Pen U.-L., 2010, Phys. Rev. D, 81, 103527
Masui K. W. et al., 2013, ApJ, 763, L20
Modi C., Castorina E., Feng Y., White M., 2019, J. Cosmol. Astropart. Phys., 2019, 024
Morales M. F., Hewitt J., 2004, ApJ, 615, 7
Morales M. F., Hazelton B., Sullivan I., Beardsley A., 2012, ApJ, 752, 137
Newburgh L. B. et al., 2014, in Stepp L. M., Gilmozzi R., Hall H. J., eds, Proc. SPIE Conf. Ser. Vol. 9145, Ground-based and Airborne Telescopes V. SPIE, Bellingham, p. 91454V
Newburgh L. et al., 2016, in Hall H. J., Gilmozzi R., Marshall H. K. , eds, Proc. SPIE Conf. Ser. Vol. 9906, Ground-based and Airborne Telescopes VI. SPIE, Bellingham, p. 11
Nuttall A. H., 1981, IEEE Trans. Acoust. Speech Signal Process., 29, 84
Olivari L. C., Dickinson C., Battye R. A., Ma Y.-Z., Costa A. A., Remazeilles M., Harper S., 2018, MNRAS, 473, 4242
Overzier R., Röttgering H., Rengelink R., Wilman R., 2003, A&A, 405, 53
Parsons A. R., Pober J. C., Aguirre J. E., Carilli C. L., Jacobs D. C., Moore D. F., 2012, ApJ, 756, 165
Paul S. et al., 2016, ApJ, 833, 213
Perley R. A., Schwab F. R., Bridle A. H., 1989
Planck CollaborationI, 2014, A&A, 571, A1
Pober J. C. et al., 2014, ApJ, 782, 66
Prasad P., Subrahmanya C. R., 2011, Exp. Astron., 31, 1
Rogers A. E. E., Bowman J. D., 2008, AJ, 136, 641
Rubart M., Schwarz D. J., 2013, A & A, 555, A117
Santos M. G. et al., 2017, MeerKAT Science: On the Pathway to the SKA (MeerKAT2016). Stellenbosch, South Africa
Sarkar D., Bharadwaj S., 2018, MNRAS, 476, 96
Sarkar A. K., Bharadwaj S., Ali S. S., 2017, J. Astrophys. Astron., 38, 14
Sarkar A. K., Bharadwaj S., Marthi V. R., 2018a, MNRAS, 473, 261
Sarkar A. K., Bharadwaj S., Sarkar T. G., 2018b, J. Cosmol. Astropart. Phys., 2018, 051
Seo H.-J., Dodelson S., Marriner J., Mcginnis D., Stebbins A., Stoughton C., Vallinotto A., 2010, ApJ, 721, 164
Sirothia S. K., Dennefeld M., Saikia D. J., Dole H., Ricquebourg F., Roland J., 2009, MNRAS, 395, 269
Subrahmanya C. R., Manoharan P. K., Chengalur J. N., 2017a, J. Astrophys. Astron., 38, 10
Subrahmanya C. R., Prasad P., Girish B. S., Somashekar R., Manoharan P. K., Mittal A. K., 2017b, J. Astrophys. Astron., 38, 11
Swarup G. et al., 1971, Nat. Phys. Sci., 230, 185
Swarup G., Ananthakrishnan S., Kapahi V. K., Rao A. P., Subrahmanya C. R., Kulkarni V. K., 1991, Curr. Sci., 60, 95
Switzer E. R. et al., 2013, MNRAS, 434, L46
Thyagarajan N. et al., 2013, ApJ, 776, 6
Thyagarajan N. et al., 2015, ApJ, 807, L28
Thyagarajan N. et al., 2015, ApJ, 804, 14
Trott C. M., Wayth R. B., Tingay S. J., 2012, ApJ, 757, 101
Vedantham H., Udaya Shankar N., Subrahmanyan R., 2012, ApJ, 745, 176
Villaescusa-Navarro F. et al., 2018, ApJ, 866, 135
Visbal E., Loeb A., Wyithe S., 2009, J. Cosmol. Astropart. Phys., 10, 030
Wyithe J. S. B., Loeb A., Geil P. M., 2008, MNRAS, 383, 1195

APPENDIX A: VARIANCE OF THE ESTIMATOR

In Section 4, we have used several statistically independent realizations of the signal to determine the variance (σ^2) of the estimated power spectrum. Such a procedure is, by and large, only possible with simulated data. We usually have accessed to only one statistically independent realizations of the sky signal, and the aim is to use this to not only estimate the power spectrum but also predict the uncertainty in the estimated power spectrum. Considering the power spectrum estimator $\hat{P}\,(\boldsymbol{U}_a, \tau_m)$, we theoretically calculate the variance

$$\sigma_{\rm p}^2(\boldsymbol{U}_a, \tau_m) = \langle \hat{P}^2\,(\boldsymbol{U}_a, \tau_m)\rangle - \langle \hat{P}\,(\boldsymbol{U}_a, \tau_m)\rangle^2\,. \tag{A1}$$

which is used to predict the uncertainty in the estimated power spectrum $P(\boldsymbol{k}_\perp, k_\parallel)$. The entire analysis here is based on the assumption that the H I signal is a Gaussian random field.

Considering the power spectrum estimator, we have

$$\sigma_{\rm p}^2(\boldsymbol{U}_a, \tau_m) = \left[P(\boldsymbol{k}_{\perp a}, k_{\parallel m}) + P_{\rm N}(\boldsymbol{k}_{\perp a}, k_{\parallel m})\right]^2\,. \tag{A2}$$

We use $\langle|\mathcal{N}'(\boldsymbol{U}_a, \nu_n)|^2\rangle = 2\sigma_{\rm N}^2(\boldsymbol{U}_a)$ (equation 11), equations (17) and (18) to simplify the noise power spectrum,

$$P_{\rm N}(\boldsymbol{k}_{\perp a}, k_{\parallel m}) = \frac{r^2\, r'\, T_{\rm sys}^2}{\tilde{\eta}\,\Delta t\, N_{\rm s}\,(N_{\rm A} - a)}\,, \tag{A3}$$

where $\tilde{\eta} = [\int A^2(\theta){\rm d}^2\theta]/[\int A(\theta){\rm d}^2\theta]^2$ is a dimensionless factor (Chatterjee & Bharadwaj 2018a). It is worth noting that the second term in the right-hand side of equation (19), which has been introduced to subtract out the noise bias in equation (16) is ignored for calculating the variance. The signal contribution from this term to the estimator is of the order of $\sim 1/N_{\rm s}$, which is extremely small for a long observation.

Fig. A1 shows the analytic prediction for the variance calculated using equation(A2) (solid line) for a total observation time of $t_{\rm obs} = 1000$ h with an integration time $\Delta t = 1$ h for the uniform illumination. For comparison, we also show (points) the variance estimated from $N_{\rm r} = 1000$ independent realizations of the simulated signal visibilities. Here we have binned the variance $\sigma_{\rm p}(\boldsymbol{U}_a, \tau_m)$ at the $(\boldsymbol{k}_\perp, k_\parallel)$ modes corresponding to the OWFA baselines and delay channels into 20 equally spaced logarithmic bins to compute $\sigma_{\rm p}(k)$. The shaded region in the figure shows the theoretically estimated error $\Delta_{\sigma_{\rm p}} = \sigma_{\rm p}(k)/\sqrt{N_{\rm r}}$ in $\sigma_{\rm p}(k)$ for $N_{\rm r} = 1000$ statistically independent realizations of the H I signal. We see that the analytic predictions

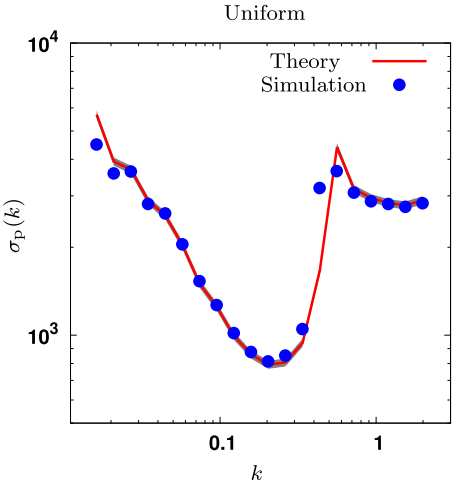

Figure A1. The analytic prediction for the variance (equation A2) for auto-correlation is compared with variance estimated from $N_{\rm r} = 1000$ realizations of the simulated signal visibilities.

are in reasonably good agreement with the values obtained from the simulations over the entire k-range that we have considered here, except the two smallest k-bins. This discrepancy possibly arises because the estimator ignores the convolution with the aperture power pattern that is included in the simulated visibility signal (equation 9). From Fig. A1, we also notice that $\sigma_{\rm p}(k)$ remains relatively small in the k-range 0.05–0.3 Mpc^{-1}, which is consistent with the findings of Sarkar et al. (2017). The k modes larger than 0.7 Mpc^{-1} remains noise dominated and larger hours of observation is required to extract signal from these modes.

This paper has been typeset from a TEX/LATEX file prepared by the author.